0D/2D Schottky junction synergies with 2D/2D S-scheme heterojunction strategy to achieve uniform separation of carriers in 0D/2D/2D quasi CNQDs/TCN/ZnIn$_2$S$_4$ towards photocatalytic remediating petroleum hydrocarbons polluted marine

Linhong Xia [a], Kaisheng Zhang [b,*], Xudong Wang [a], Qi Guo [a], Yuning Wu [a], Yujie Du [a], Lixue Zhang [a], Jianfei Xia [a], Hua Tang [c], Xia Zhang [d], Yanhua Peng [a], Zhuo Li [a,*], Xiaolong Yang [a,*,1]

[a] *School of Chemistry and Chemical Engineering, State Key Laboratory of Bio-fibers and Eco-textiles, Collaborative Innovation Center of Shandong Marine Bio-based Fibers and Ecological textiles, Qingdao University, 308 NingXia Road, Qingdao 266071, PR China*
[b] *Environmental Materials and Pollution Control Laboratory, Institute of Solid State Physics, HFIPS, Chinese Academy of Sciences, Hefei 230031, PR China*
[c] *School of Environmental Science and Engineering, Qingdao University, Qingdao 266071, PR China*
[d] *School of Chemistry and Chemical Engineering, Henan University of Technology, Zhengzhou 450001, PR China*

ARTICLE INFO

ABSTRACT

The inherent advantages of 2D/2D S-scheme heterojunction contribute well to the photocatalysis due to efficient carriers' separation kinetics and maintained redox ability. However, single 2D/2D S-scheme heterostructure fails to realize a perfect energy band alignment since the material contact interface is not perfectly contacted in real circumstance because of surface roughness and flexibility of 2D material. Herein, the 0D/2D Schottky junction synergies with S-scheme (S-S strategy) is proposed to improve weak links above. 0D Quasi CNQDs are utilized in 2D/2D S-scheme TCN/ZnIn$_2$S$_4$ to optimize the carriers' separation kinetics in some area without 2D/2D close contact for TCN/ZnIn$_2$S$_4$. SI-XPS, UPS, and KPFM etc confirms such electron state. The CNQDs/TCN/ZnIn$_2$S$_4$ photocatalysts exhibits high degree of dissociation efficiency of photoinduced excitons due to S-S strategy. The results testify construction of S-S heterostructure would be an effective strategy for carriers' modulation, and it will be a promising candidate for "green" elimination of oil spill on water surface.

1. Introduction

Human being's rapid demand for energy, especially oil and other fuels, increasing the risk of oil leakage in the process of exploitation, transportation and refining. Marine oil spill severely threatens the marine ecological environment and deteriorate the ecosphere of earth eventually. From Exxon Valdez in 1989 to oil tanker Sanchi in 2018, the oil spill occurred to date has been disastrous [1]. In addition to physical adsorption, chemical emulsification and biodegradation, the photocatalytic in-situ remediation of petroleum hydrocarbons contaminated areas has attracted extensive attention recently because of environment friendly, solar energy-driven, no secondary pollution and low cost etc [2].

Graphene-like carbon nitride (g-C$_3$N$_4$) is considered as a promising environmental function materials because of excellent stability, toxicity-free, easy-modulation and facile synthesis process, which have been widely applied in treatment of dye wastewater, antibiotics wastewater, organics contaminated soil, heavy metal pollution and antibacterial fields, etc [3–5]. Recently, our group has continuously reported elemental doping combined with defects strategy, which would be an alternative guiding ideology to synthesize high-performance g-C$_3$N$_4$ catalysts for photocatalytic degradation of n-tetradecane in water [6,7]. While large Frankel excitons binding energy still leads to high degree of recombination and subsequent low utilization efficiency of photo-induced carriers of carbon nitride [8–10].

Recently, Yu et al. [11] proposed S-scheme (step-scheme)

---

heterojunction which consisting of a reduction photocatalyst and an oxidation photocatalyst with staggered band structure based on traditional Z-scheme. Different from the previous Z-scheme (Fig. S1a and b), S-scheme heterojunction could not only efficiently separate photogenerated carriers but also maintain the redox ability of two semiconductor without sacrifices (Fig. S1c). Various g-C$_3$N$_4$-based S-scheme photocatalyst have been developed including O-doped g-C$_3$N$_4$/N-doped Nb$_2$O$_5$, ZnIn$_2$S$_4$/g-C$_3$N$_4$, CeO$_2$/PCN, WO$_3$/g-C$_3$N$_4$ and others aiming to solve problems above [12–15]. As a representative semiconductor of ternary metal sulfide, ZnIn$_2$S$_4$ has hit the limelight owing to its narrow bandgap (~2.02–2.59 eV, be able to absorb light with wavelengths up to 614 nm), rapid electron transfer ability (benefit from its inherent two-dimensional (2D) layered structure) and facile synthesis approach [16]. Huang et al. devised ZnIn$_2$S$_4$ nanosheets@g-C$_3$N$_4$ core–shell architecture, which could simultaneously exploit 2D/2D morphology advantage as well as S-scheme charge modulation mechanism [15]. Such ZIS/g-CN structure was also reported as direct or indirect Z-scheme by other groups. Bai et al. proposed ultrathin 2D ZnIn$_2$S$_4$/g-C$_3$N$_4$ Z-scheme heterojunction to boost interfacial charge separation in 2D Z-scheme heterojunction for PHE [17]. Wang et al. also found 2D/2D g-C$_3$N$_4$/ZnIn$_2$S$_4$ S-scheme heterojunction exhibited excellent redox capability for tetracycline degradation [18].

Unfortunately, the chemical synthesis process often fails to realize perfect contact of different material interfaces at nano level in real circumstance. In addition, some flexible material like ultrathin ZnIn$_2$S$_4$ nanosheets tend to wrinkle during the assembling process. In this case, 2D/2D interface would not be perfectly contact in some places, that way S-scheme heterojunction do not produce a marked effect compared with intimately contacting area and point [19–21]. As a result, the advantage of S-scheme is reduced great. Specifically charge dynamics is regulated

in the close interfacial region of binary materials, while charge dynamics is not effectively promoted far away from the intimated binary material interface (Scheme 1).

Therefore, herein 0D components CNQDs are introduced to the 2D/2D g-C$_3$N$_4$/ ZnIn$_2$S$_4$ S-scheme heterojunction to construct Schottky junction, which cooperates with every component of S-scheme heterojunction to reach the effect that 1 + 1 is greater than 2 (Scheme 1). Be specifically, firstly the built-in electric field (BIEF) of 2D/2D S-scheme efficiently regulates the separation kinetics of photogenerated carriers in the close contact region; secondly Schottky junction rely on 0D material (0D/2D) regulates photogenerated charge's separation kinetics far from the close contact regions of 2D/2D g-C$_3$N$_4$/ZnIn$_2$S$_4$ [22]. Such S-S strategy combined material interfacial spatial structure with corresponding charge carrier's transfer path, which is an effective supplement to the 2D/2D S scheme strategy.

Guided by the S-S strategy herein 0D/2D/2D (or 0D/2D/3D from macroscopic view) quasi CNQDs/ tubular g-C$_3$N$_4$/ZnIn$_2$S$_4$ were synthesized by facile one-step process, which exhibited superior photocatalytic degradation activity towards petroleum hydrocarbons in seawater under visible light illumination. Various physical chemical characterization methods have been conducted to explore the inherent properties including Synchronous irradiation XPS (SI-XPS), Ultraviolet photoelectron spectroscopy (UPS) as well as Kelvin probe force microscopy (KPFM) etc. Combined with the corresponding characterization results, it is proposed the intrinsic reason for the superior catalytic activity of quasi CNQDs/TCN/ZnIn$_2$S$_4$ heterojunction was attributed to efficient separation kinetics of photoinduced carriers of designed S-S strategy in every contact point or face (0D/2D CNQDs/TCN, 0D/2D CNQDs/ZnIn$_2$S$_4$, 2D/2D TCN/ZnIn$_2$S$_4$). It implies that Schottky junction cooperates with S-scheme junction would be an effective strategy for
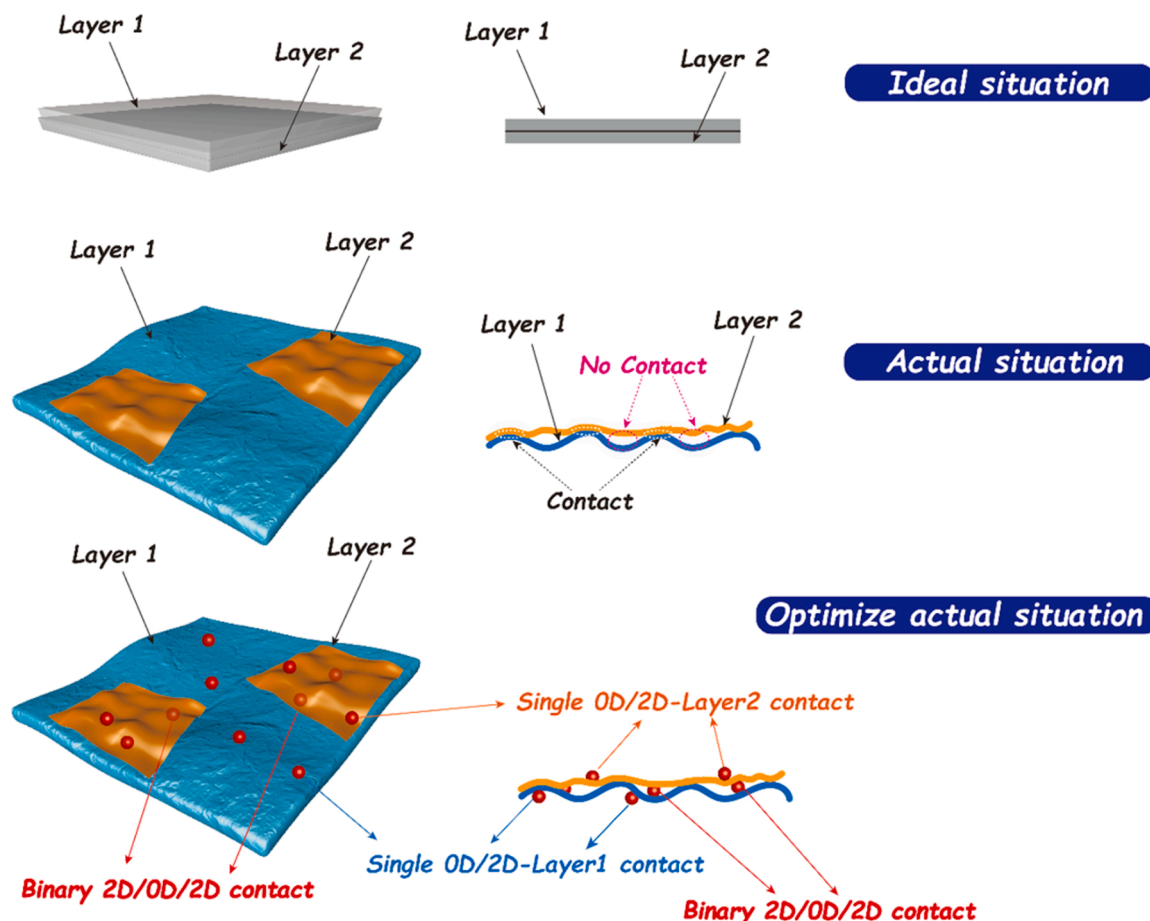
Scheme 1. Utilization of Schottky junction cooperated with S-scheme heterojunction to optimize actual situation of carriers' separation behavior.

carriers' modulation in 0D/2D/2D CNQDs/TCN/ZnIn$_2$S$_4$ heterostructure, which could serve as a promising candidate for "green" elimination of oil spill simultaneously.

2. Experimental section

2.1. Preparation procedure

2.1.1. Preparation of CZ

CZ: CZ were prepared by solvothermal method. Briefly, 0.3 g TCN was fully dispersed into 30 mL of ethanol and deionized water (V_{H2O}: $V_{CH3OH} = 1:1$). Subsequently, 0.28 mmol ZnCl$_2$, 0.56 mmol InCl$_3$·4H$_2$O and 2.24 mmol TAA (M_{Zn}:M_{In}:M_S = 1:2:8) were dissolved into the above mixed solution. The solution was stirred vigorously for 30 min and transferred to 100 mL Teflon-lined autoclave, which was solvothermal treated for 12 h at 160 °C. The earth-yellow sample was recovered by filter, wash and dry procedure. The earth-yellow powder was marked as CZ40. A series of CZ-x (x = 20, 30, 40, 50) with x wt% ZnIn$_2$S$_4$ loading amount were prepared by adjusting the added amount of precursor of ZnIn$_2$S$_4$.

2.1.2. Preparation of CNQDs/CZ

CNQDs/CZ: The prepared CNQDs was dispersed in water by ultrasound for 30 min. The concentration of prepared CNQDs suspension was 5 mg/mL for further employ. The preparation mechanism of CNQDs/CZ was illustrated in Fig. 1a. Take 2CNQDs/CZ40 as an example. Concretely, 0.3 g of TCN was fully dispersed into 30 mL of ethanol and deionized water (V_{H2O}:$V_{CH3OH} = 1:1$). Subsequently, 0.28 mmol ZnCl$_2$, 0.56 mmol InCl$_3$·4H$_2$O and 2.24 mmol TAA (M_{Zn}:M_{In}:M_S = 1:2:8) were dissolved into the above mixed solution. Simultaneously, 1.2 mL CNQDs suspension was transferred to the above solution and stirred vigorously for 30 min. Ultimately, the mixed solution was transferred to 100 mL Teflon-lined autoclave and kept at 160 °C for 12 h. The green sample was recovered by filter, wash and dry procedure. The green powder was marked as 2CNQDs/CZ40. Thus, a series of CNQDs/CZ40 were prepared by adjusting the added amount of CNQDs suspension and marked as x-CNQDs/CZ40 (x = 0.5, 2, 3, 5) with x wt% CNQDs loading amount.

The preparation procedures of other samples including TCN, ZIS, Quasi CNQDs CNQDs/TCN and CNQDs/ZIS were attached in S1.2.

2.2. Characterization methods

The X-ray diffractions (XRD) were conducted on Ultima IV (Rigakum, Japan) with Cu K$_\alpha$ irradiation ($\lambda = 0.15418$ nm), and the diffraction angles was set in range of 5–80°. The FT-IR spectra were detected by Nicolet is50 (Thermo, USA). The SEM images were photographed using Hitachi SU8010 (JOEL, Japan). The TEM, HRTEM, EDS and element mapping images were photographed using JEM-F200 at 200 kV voltage (JOEL, Japan). The XPS spectra were carried out in Escalab 250Xi (Thermo, USA) with Al-K$_\alpha$ (hν=1486.6 eV). The in-situ illumination XPS with visible light irradiation ($\lambda > 420$ nm) was conducted on Escalab Xi+ (Thermo, USA), all XPS spectra were corrected via C 1 s of adventitious carbon at 284.8 eV. The UPS spectra were conducted on Escalab Xi+ (Thermo, USA). The UV–Vis DRS was conducted with SPECPRD 210 Plus (Jena, Germany) using BaSO$_4$ as background. The PL spectra were operated on FLS 980 (Ediburgh, England), and all samples were excited by continuously adjustable Xe-lamp at 375 nm and ambient temperature. The KPFM images were operated on Cypher S (Asylum Research, USA) using ASYELEC.01-R2 as conductive probe with 25 nm tip radius. The in-situ ESR signals were collected at 0 and 10 min under visible light irradiation ($\lambda > 420$ nm) on A300 (Bruker, Germany). The photoelectrochemical tests were operated on PARSTAT 4000 A (Princeton, USA).

2.3. Photocatalytic degradation of n-tetradecane

The photocatalytic experiment was based on the previous work [6]. The spilled oil was represented by n-Tetradecane (C14). The device of photocatalytic degradation was shown in Fig. S2. Specifically, 100 mg photocatalyst were dispersed into 10 mL deionized water containing 50 mg C14 (c(C14) = 5 g/L) dwelt in double jacket reactor. The suspension was stirred for 30 min in the dark with a speed of 1300 rpm to ensure full contact. Subsequently, visible light with 550 mW/cm^2 (Throlabs PM100D, USA, Fig. S3) top-illuminated was conducted on reactor from 300 W Xe-lamp (CEL-PF300-T8, China Education Au-light) with 420 nm cut-off filter (Fig. S4). The reaction was conducted at room temperature by connected the condensate. The residual C14 extracted with dichloromethane was detected and quantified by GC-FID (HP-5 capillary column, Kejie GC5890N, China) and method with n-Decane (C10) as internal standard (see S1.4 in SI). The reaction intermediates during degradation process were further detected and analysis by GC-MS (see S1.8 in SI).

3. Results and discussion

3.1. Characterization and analysis

The bulk structure of series photocatalysts are characterized by XRD. As shown in Fig. 1b, two characteristic peaks appear at 13.2° and 27.4° are observed in tubular g-C$_3$N$_4$ (TCN), corresponding to intralayer ordered-arranged heptazine units (100) as well as interlayer stacked heptazine structure (002), respectively (Pink Heart). Six characteristic peaks located at 6.6°, 21.5°, 27.7°, 30.4°, 47.3° and 52.2° in ZnIn$_2$S$_4$ are attributed to (002), (006), (102), (104), (110) and (1012) planes, respectively (Brown Diamond), indicating its hexagonal ZnIn$_2$S$_4$ (JCPDS No.72–0773). As a typical representative of TCN/ZnIn$_2$S$_4$, CZ40 exhibits characteristic peaks of both g-C$_3$N$_4$ and ZnIn$_2$S$_4$. Significantly, diffraction peak of (100) lattice facet shifts to 11.1° compared with pristine TCN, which may be ascribed to intralayer arrangement of N-lined heterocyclic ring during one-step solvothermal process [23]. In addition, quasi CNQDs shows two peaks locates at 27.3° and 9.3°, which are indexed to characteristic (002) and (100) facet of g-C$_3$N$_4$. The latter diffraction peak shifts to low-angel direction, which is ascribed to the formation of triazine based structure (PTI) at quantum size with an increased distance (d=0.95 nm) between unit structure (Fig. S5) [24]. Furthermore, CNQDs/CZ40 exhibits similar pattern with CZ40, which may be attributed to low loading amount or low crystallinity of quasi CNQDs.

The surface functional group of photocatalysts are investigated by FTIR. As shown in Fig. 1c, the FTIR spectra of CZ40 confirms the combination of TCN with ZnIn$_2$S$_4$ nanosheets. The broad peaks at 3700–3000 cm^{-1} originate from the surface-adsorbed water and terminal amino groups of the samples. Prominent absorption band at 1200–1650 cm^{-1} and 804.6 cm^{-1} is attributed to typical stretching vibration of tri-s-triazine ring units and characteristic peak of breathing vibration mode of C−N of heptazine in TCN, respectively [25]. The new absorption peak at 1079.1 cm^{-1} is assigned to stretching vibration of C-O bond due to hydroxylation of -OH grafted into the TCN by solvothermal treatment in CZ40 and 2CNQDs/CZ40 [26]. The absorption peak of CNQDs focuses on 1576.7 cm^{-1} and 842.7 cm^{-1}, which are ascribed to tensile vibration of C=N and breathing vibration of triazine [23,27]. Remarkably, the intensity of bending vibration of C-NH-C (735.7 cm^{-1}) is stronger, and the content of C-NH-C is increased in PTI-based structure in quasi CNQDs [28]. The CNQDs/CZ40 remains the same FTIR pattern with that of CZ40.

The micro-morphology of samples is presented on FESEM, TEM and HRTEM images. As illustrated in Figs. 1d, e and S6a, b, the representative marigold-shaped flow-like sphere of ZnIn$_2$S$_4$ is observed, simultaneously TCN exhibits hexagonal hollow tubular morphology [29]. As shown in Figs. 1f, 2a, b and S6c, CZ40 exhibits unique morphology that
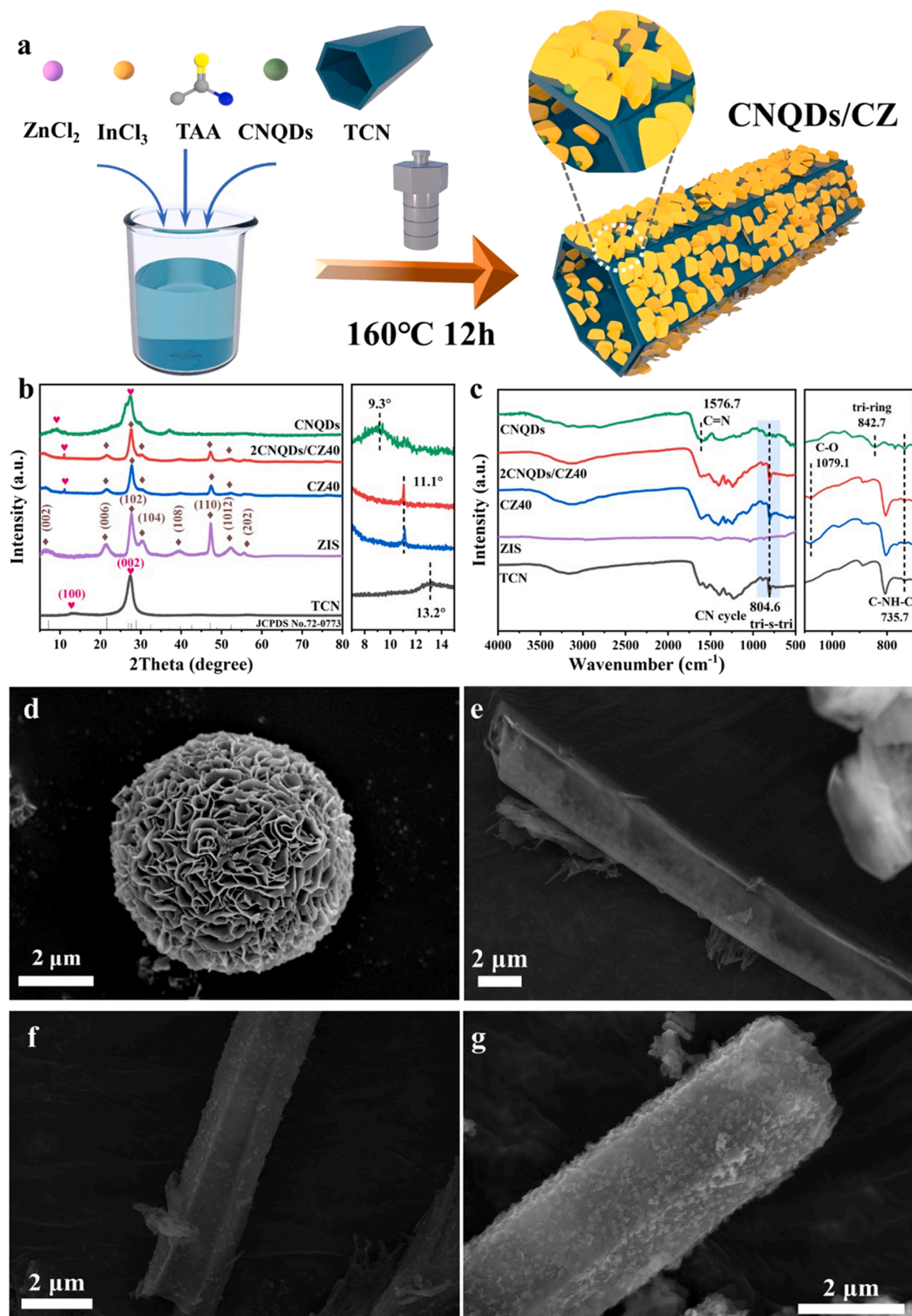
Fig. 1. (a) Schematic illustration of preparation processes of 2CNQDs/CZ40; (b) XRD patterns, enlarged XRD patterns in the 2θ range of 7–15°; (c) FT-IR spectra, enlarged FT-IR spectra in the wavenumber range of 700–1100 cm^{-1}; FESEM images of (d) ZIS, (e) TCN, (f) CZ40 and (g)2CNQDs/CZ40.
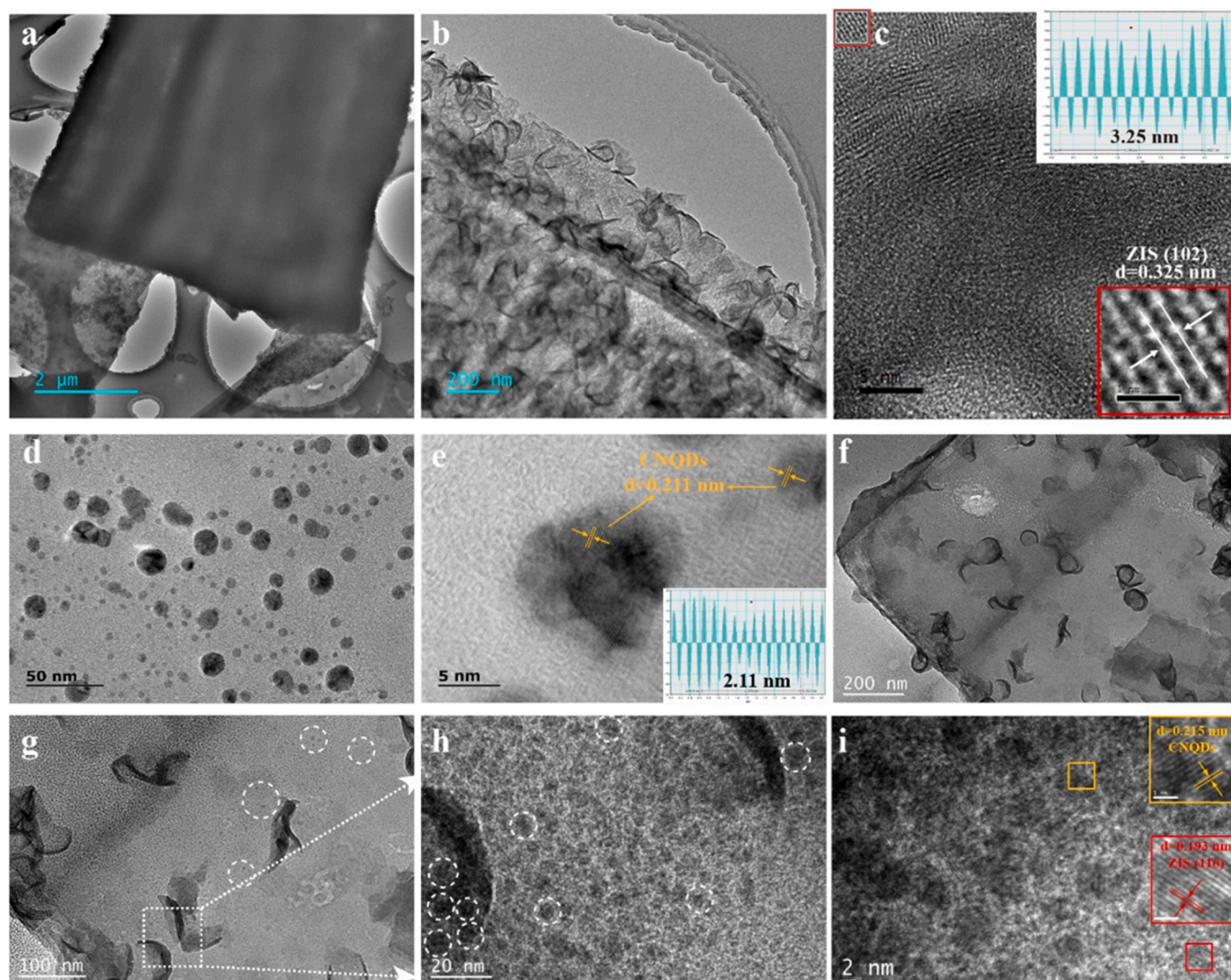
Fig. 2. TEM images of (a, b) CZ40, (d) CNQDs, (f, g, h) 2CNQDs/CZ40; HRTEM and FFT images of (c) CZ40, (e) CNQDs; (i) HRTEM image of 2CNQDs/CZ40.

fish-scale $ZnIn_2S_4$ grown on the inner and outer surface of TCN. Such intimated contact between $ZnIn_2S_4$ and TCN contributes to the formation of the interfacial electron transfer region [30]. The HRTEM images of CZ40 show inferior crystallinity of TCN and clear lattice fringe of 0.325 nm, which is attributed to (102) lattice plane of hexagonal phase $ZnIn_2S_4$ (Fig. 2c). As shown in Fig. 2d, quasi CNQDs with diameter of 5–10 nm is obviously observed without agglomeration. The lattice fringe of quasi CNQDs is 0.215 nm as shown in Fig. 2e. Similar with FESEM results (Figs. 1g and S6d), fish-scale $ZnIn_2S_4$ nanosheets anchored on the surface of TCN material, in addition, anchored CNQDs could observed in the white circle area (Fig. 2f, g). Enlarging the white square area of Fig. 2g, it is observed that abundant CNQDs are uniformly attached to the interfaces of single TCN, single $ZnIn_2S_4$ and $ZnIn_2S_4$/TCN (Fig. 2h). The lattice fringe of 0.215 nm corresponding to CNQDs are accurately found in Fig. 2i, and that of 0.193 nm corresponding to (110) planes of $ZnIn_2S_4$ are located around CNQDs (FFT images shown in Fig. S7). Next, the amorphous region is TCN, confirming that CNQDs are fixed at the interface between TCN and $ZnIn_2S_4$, which facilitates interfacial migration of charges. The AFM results further confirmed such insertion appearance of CZ40 or 2CNQDs/CZ40. As shown in Fig. S8, the thickness of TCN and $ZnIn_2S_4$ are about 10 and 38 nm respectively. Apparently CZ40 and 2CNQDs/CZ40 exhibit an average thickness of 15–17 nm, indicating $ZnIn_2S_4$ is obliquely inserted on TCN at different angles and the gaps are filled with CNQDs. As shown

in Fig. S9, it is confirmed C, N and O elements distribute uniformly and Zn, In, and S elements distribute mainly on the fish-scale region for 0D/2D/2D 2CNQDs/CZ40 heterojunction photocatalyst.

The optical absorption properties of samples are investigated at 300–800 nm by UV–vis DRS. As shown in Fig. 3a, the absorption band edge of TCN locates at visible region about ~460 nm with gray-yellow appearance. $ZnIn_2S_4$ exhibits stronger visible light absorption ability with cut-off band edge of ~600 nm. As illustrated in Fig. 3b, the band gap (E_g) of TCN and $ZnIn_2S_4$ are determined to be 2.78 and 2.29 eV through Tauc method (See S2.1 in SI for detailed calculation), respectively. Compared to TCN material, CZ40 exhibits enhanced visible light absorption ability, which is also reflected by its light-yellow appearance. CNQDs shows excellent broad-spectral photon absorption capability in the range of 300–800 nm, correspondingly such superior visible light absorption ability is great enhanced by the introduction of CNQDs to 2CNQDs/CZ40 photocatalyst. Accordingly, its color changes from light yellow for CZ40 to chartreuse for 2CNQDs/CZ40.

The Mott-Schottky plots and UPS tests are employed to investigate the energy band structure of samples. As illustrated in Fig. 3c, the Mott-Schottky plots of samples are measured at frequency of 1000 Hz, the corresponding flat-band potentials of TCN and $ZnIn_2S_4$ are estimated to be − 0.09 and − 0.7 eV (vs. NHE). Both TCN and $ZnIn_2S_4$ are n-type semiconductors since the positive slope of the fitted M-S curve. Generally, the conduction band potential (CB) of the n-type semiconductor is
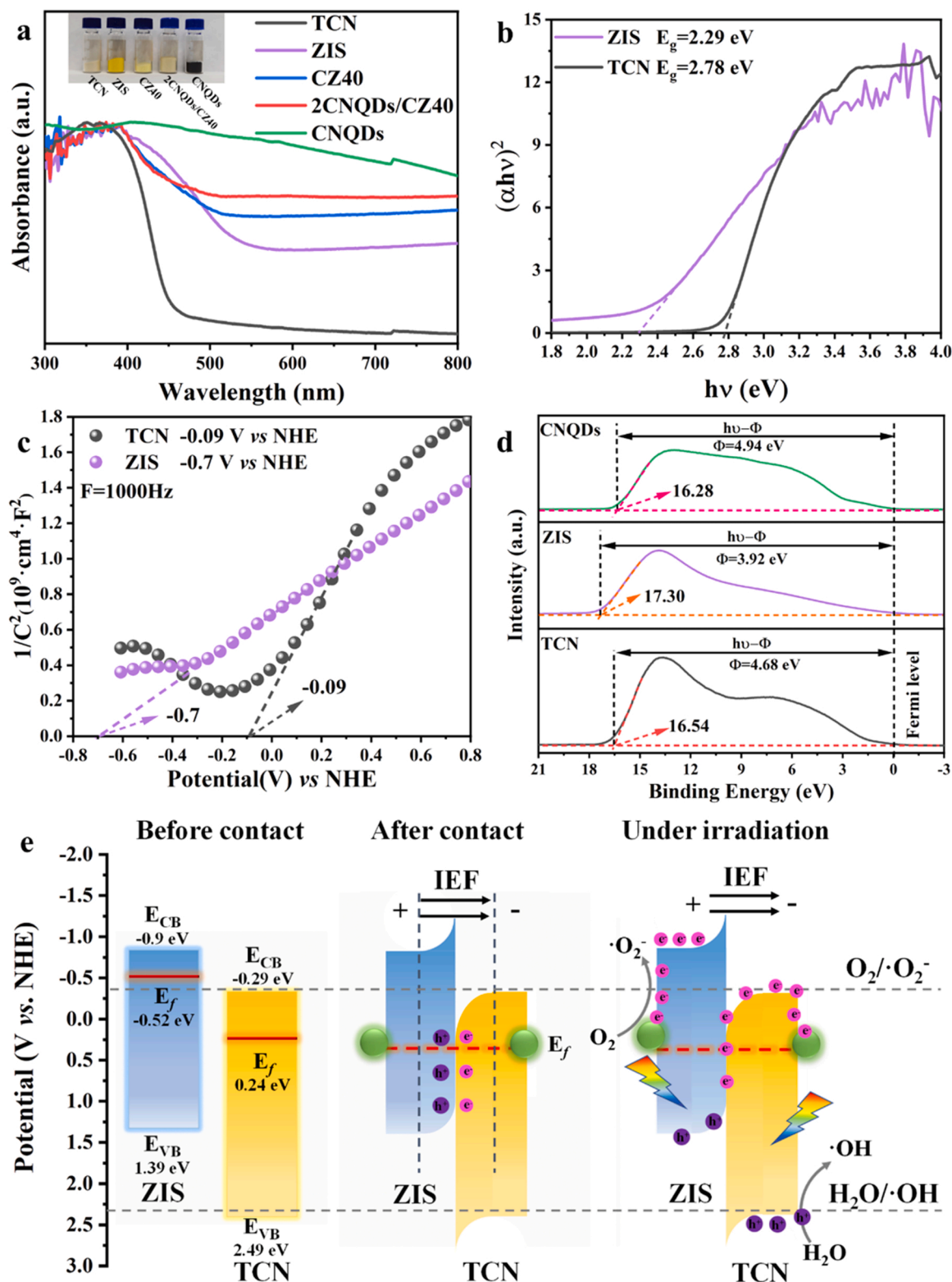
Fig. 3. (a) UV–Vis DRS spectra and (b) Tauc plots of samples; (c) Mott-Schottky plots of TCN and ZIS; (d) UPS spectra of samples; (e) Schematic illustration of TCN and ZIS band structure in before contact and after contact, and S-scheme charge-transfer pathway under irradiation.

0.2 eV more negative than the flat band potential (FLB). Thus, the CB are determined to be − 0.29 and − 0.9 eV (vs. NHE) for TCN and $ZnIn_2S_4$, respectively. The valence band potential (VB) is easily calculated with M-S plots (CB) and Tauc results (Eg). As shown in Fig. 3e, the energy band structural scheme is obtained, the VB of $ZnIn_2S_4$ locates at 1.39 eV (vs. NHE), which cannot meet the require of generation of hydroxyl

radical •OH from H_2O or OH^- species (E [H_2O/•OH] = 2.40 eV vs. NHE). But its CB (−0.9 eV) is negative enough to drive single electron reduction process of O_2 (E [O_2/•O_2^-] = −0.33 eV vs. NHE). By contrast, the VB of TCN (2.49 eV vs. NHE) is positive enough to produce hydroxyl radical •OH, while the CB of TCN (−0.29 eV vs. NHE) cannot reduce O_2 to produce superoxide radicals •O_2^-. Therefore, the $ZnIn_2S_4$ as reductive

photocatalyst and TCN as oxidative photocatalyst can be combined in S-scheme heterojunction to reserve excellent redox ability. As a results, such complementary semiconductor material with matching oxidation type and reduction type is an excellent candidate for forming the S-scheme, which can make full use of the oxidation ability and reduction ability of the above two semiconductors (TCN, $ZnIn_2S_4$), thereby improving the effective utilization efficiency of photogenerated carriers in the photocatalytic reaction.

Furthermore, the work function (Φ) as well as Fermi energy level (E_f) are determined by UPS. As shown in Fig. 3d, the work function (Φ) of samples is estimated to 4.68, 3.92 and 4.94 eV (vs. vacuum) for TCN, $ZnIn_2S_4$ and CNQDs respectively (See S2.1 in SI for detailed calculation) [31,32]. The Φ is equivalent to E_f energy. Subsequently, the E_f of TCN, $ZnIn_2S_4$ and CNQDs are converted to 0.24, $-$ 0.52 and 0.50 eV (vs. NHE) respectively, according to equation: $E_{NHE}=E_{vac}-4.44$ eV [33]. After close contact, electron of $ZnIn_2S_4$ tend to flow to TCN due to the difference in work function until the Fermi level is leveled [34]. Thus, built-in electronic field (BIEF) are constructed spontaneously at the interface with the direction from $ZnIn_2S_4$ to TCN. Simultaneously, E_f of CNQDs is much negative than that of $ZnIn_2S_4$ and TCN, CNQDs anchored on the surface of $ZnIn_2S_4$ and TCN promote the inherent electron flow from them to CNQDs [26,35], thus Schottky junction are formed far away from the TCN/$ZnIn_2S_4$ interface. Therefore, once under irradiation, $ZnIn_2S_4$ and TCN would be excited by visible light, photoinduced electrons accumulated on the CB of TCN would flow to VB of $ZnIn_2S_4$ under BIEF driven force in TCN/$ZnIn_2S_4$ interface (S-scheme), further, electrons excited on the CB of sole $ZnIn_2S_4$ and TCN would flow to CNQDs spontaneously (Schottky), thus S-scheme in the close contact region of CN/ZIS interface and Schottky junctions far away from the TCN/ZIS interface would collectively efficiently regulate the separation kinetics of photogenerated carriers everywhere (Fig. 3e).

Afterward, Kelvin probe force microscope (KPFM) is employed to obtain an in-depth understanding of the interfacial charge transfer behavior of 2CNQDs/CZ40 photocatalyst. As shown in Fig. 4, contact potential difference (CPD) of the samples in dark condition are measured. The average surface potential of TCN (31.28 mV) increases to 63.96 mV for CZ40 after it is coupled with $ZnIn_2S_4$ (19.45 mV) because the surface energy band of $ZnIn_2S_4$ would bend upward to form a S-scheme junction with TCN whose surface energy band bends downward. Such intensity of inherent BIEF would further increase after the decoration of CNQDs in surface of CZ40, the surface potential of CZ40/CNQDs reaches 126.3 mV, almost twice that of CZ40, which is probably attributed to interface Schottky structure formed by the introduction of CNQDs with large work function [36].

The surface elemental chemical environment of catalysts is determined by XPS technique. As shown in Fig. 5a, Zn, In, S from $ZnIn_2S_4$ and C, N, O signal peaks from TCN as well as CNQDs are all observed from XPS survey of 2CNQDs/CZ40, which is consistent with the element composition detected by TEM-EDX spectra of 2CNQDs/CZ40 (Fig. S9). The Zn 2p spectra (Fig. 5b) of the CZ40 and 2CNQDs/CZ40 at 1045.0 eV and 1022.1 eV belong to Zn $2p_{1/2}$ and Zn $2p_{3/2}$, respectively. It confirms Zn^{2+}. Compared with pure $ZnIn_2S_4$, the binding energies of Zn $2p_{1/2}$ and Zn $2p_{3/2}$ of CZ40 and 2CNQDs/CZ40 are decreased ($\Delta = 0.2$ eV). In Fig. 5c, the two peaks at 452.3 eV (In $3d_{3/2}$) and 444.8 eV (In $3d_{5/2}$) in In 3d spectrum are ascribed to In^{3+}. In Fig. 5d, the two peaks of S $2p_{1/2}$ and S $2p_{3/2}$ located at 162.45 eV and 161.3 eV. Compared with pure $ZnIn_2S_4$, the binding energy of S $2p_{1/2}$ and S $2p_{3/2}$ of CZ40 and 2CNQDs/CZ40 increase ($\Delta = 0.2$ eV). Significantly, Zn 2p and S 2p of CZ40 and 2CNQDs/CZ40 all move slightly towards lower binding energies direction than those of pure $ZnIn_2S_4$, indicating the presence of strong interfacial interactions between $ZnIn_2S_4$ and TCN[37,38] .

As shown in Fig. 5e, the C 1 s spectrum of TCN exhibits four peaks at 284.8, 286.4, 288.2 and 289.2 eV, which are attributed to standard carbon (C-C/C=C), terminal amino groups-bonded carbon (C-NH$_X$), sp^2-hybridized carbon of heptazine units (N-C=N) and carbon bonded to oxygen (C-O/C=O), respectively [39]. It is obviously the contribution of "C-O/C=O" increased significantly from 2.6% (TCN) to 7.91% (CZ40) and 8.56% (2CNQDs/CZ40) (Table S1), respectively, which is
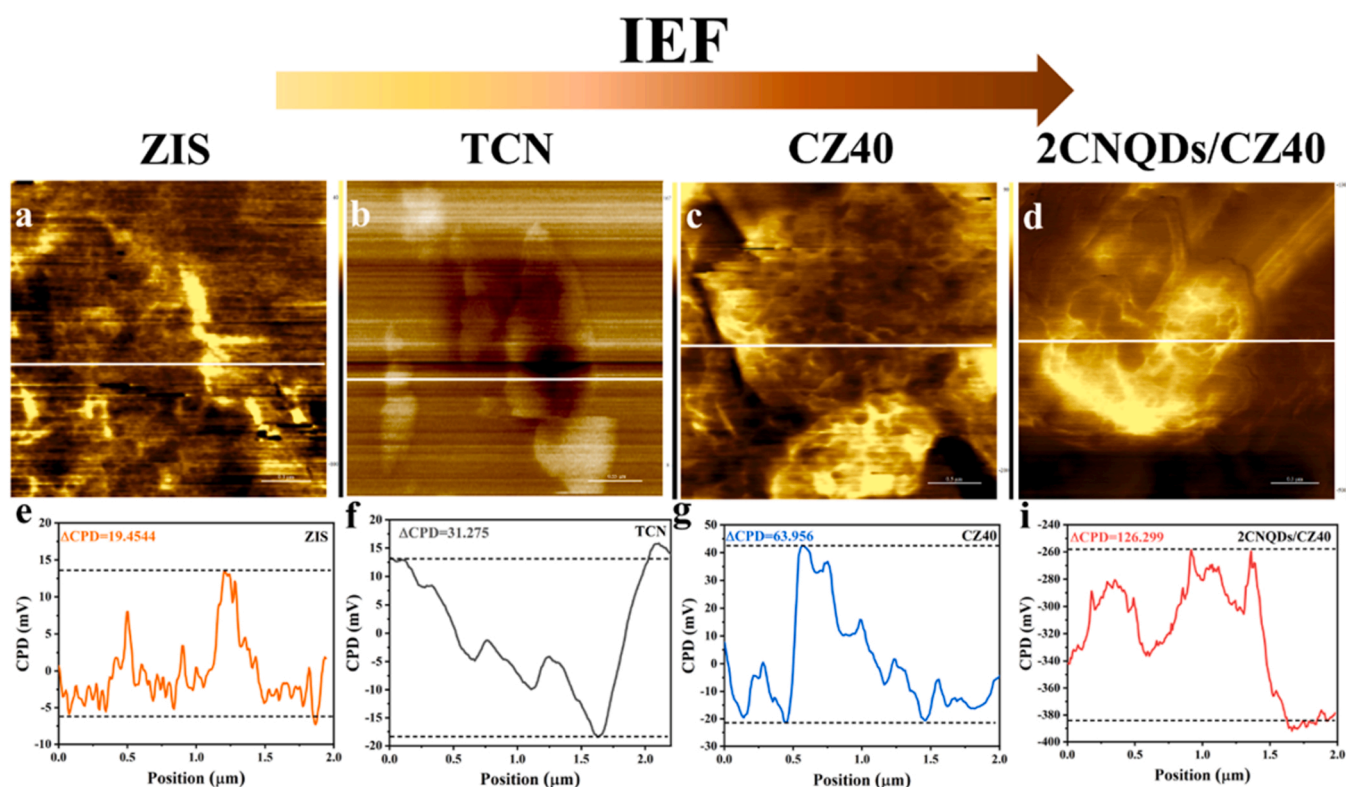

Fig. 4. KPFM images of (a) ZIS, (b) TCN, (c) CZ40 and (d) 2CNQDs/CZ40; the contact potential difference distributions of the line profiles in (e) ZIS, (f) TCN, (g) CZ40 and (i) 2CNQDs/CZ40.
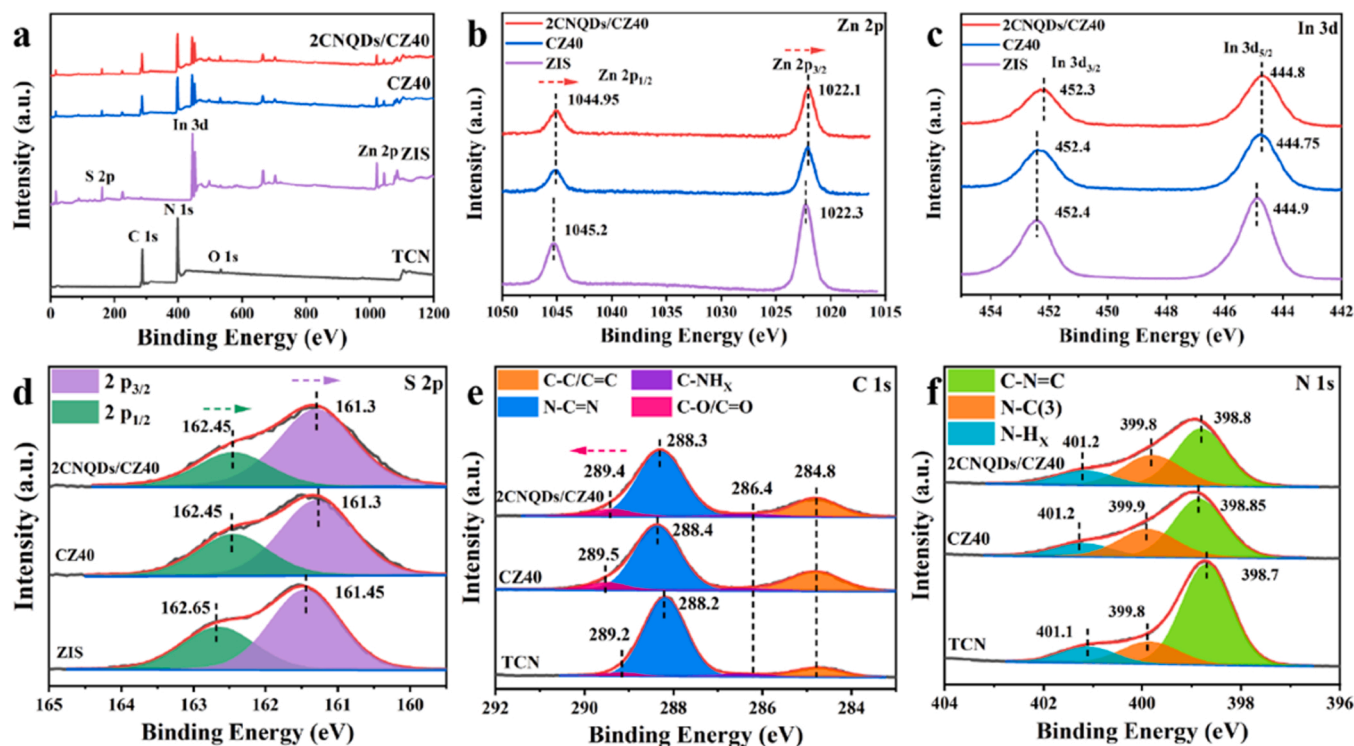
Fig. 5. (a) XPS survey spectrum of samples; High-resolution XPS (b) Zn 2p, (c) In 3d, (d) S 2p, (e) C 1s and (f) N 1s spectrum of samples.

consistent with the results of Fig. 1c. At the same time, such "C-O/C=O" peak shifts about ~0.3 eV towards higher binding energy direction in CZ40, which indicates density of electrons cloud decrease compared to pristine TCN [40]. Significantly, it is reasonable to deduce the electron of carbon atom in heptazine units in TCN tend to migrate to Zn-S4 in $ZnIn_2S_4$ nanosheets driven by BIEF in S-scheme 2CNQDs/CZ40 hetero-junction under the excitation of X-ray [41], which is either testified by DFT results by other researchers [39]. Furthermore, the BE value of "C-O/C=O" of 2CNQDs/CZ40 is 0.1 eV lower than that of CZ40, which is due to the formation of Schottky junction. The electrons from TCN semiconductor tend to be enriched in CNQDs, leading to the BE value decrease compared with CZ40 [42]. The incorporation of CNQDs is also supported by the increase of "C-O/C=O" in CNQDs/CZ40 (8.56%) compared with CZ40 (7.91%), excess of O content is introduced by more edge oxygen groups grafted triazine ring of CNQDs. N 1 s spectrum of TCN is deconvoluted into triplet peaks at 398.7, 399.8 and 401.1 eV, which are assigned to the sp²-hybridized N atoms of heptazine rings (C=N-C), bridged N (N-(C)₃) and amino N (N-(H)ₓ x = 1,2), respectively (Fig. 5f). N1s of CZ40 and CNQDs/CZ40 remain the same as pristine TCN, which indicates N atoms do not take part in the interfacial charge transfer process.

Synchronous illumination X-ray photoelectron spectroscopy (SI-XPS) technique are conducted to investigate the charge transfer process of 2CNQDs/CZ40 before and after illumination (Fig. 6a and b). As shown in Fig. 6c-e, the peaks of Zn 2p shift to a low binding energy (~0.2 eV) after visible light irradiation, there is no major deviation in the peak position of In 3d and S 2p in 2CNQDs/CZ40 before and after illumination. As we discussed above (Fig. 5e), the C 1 s spectrum for 2CNQDs/CZ40 presents quadruple peaks at 284.8, 286.4, 288.3 and 289.4 eV, assigning to standard carbon, C-NRₓ, N-C=N and C-O/C=O, respectively (Fig. 6f). After visible light irradiation, the peaks of N-C=N and C-O/C=O bond shift to a high binding energy, indicating a photogenerated electrons transfer from the TCN to the $ZnIn_2S_4$. There is no major deviation in the peak position of N 1 s in 2CNQDs/CZ40 before and after illumination (Fig. 6g). Significantly, as shown in Fig. 6h, O 1 s could be deconvoluted into two peaks including hydroxyl groups bonded to carbon (C-OH) and

aldehyde oxygen (C=O) located at 531.7 and 532.8 eV, respectively. The O 1 s peaks shift to a high binding energy about ~0.1 eV, further demonstrating the photogenerated electrons migration through the novel "C-O···S-Zn" charge transfer channel between TCN and $ZnIn_2S_4$. As depicted in Fig. 6i, the photogenerated electrons accumulated on CB of TCN migrate to VB of $ZnIn_2S_4$ to recombine with photoinduced holes accumulated on VB of $ZnIn_2S_4$ through the novel "C-O···S-Zn" charge transfer channel driven by BIEF in 2CNQDs/CZ40 heterojunction under irradiation [43,44].

The recombination extent of photogenerated carriers in samples are investigated by steady-state photoluminescence (SSPL) and nanosecond level time resolved transient photoluminescence spectroscopy (TRPL) technique (Fig. 7a and b). Under the excitation wavelength of 375 nm, TCN exhibits a broad emission peak center at 465 nm because of free-electron recombination caused by electron transition from the excited state to the ground state of g-C₃N₄. The emission peak is well corresponding to its absorption band edge as shown in Fig. 3a. The hexagonal $ZnIn_2S_4$ is not a strong photoluminescence material owing to its weak binding energy of Winner exciton [45], thus pristine $ZnIn_2S_4$ exhibits negligible emission peak not only under such excitation condition, but also under the excitation wavelength of 430 nm or 470 nm (Fig. S11). Remarkably, the superior conductivity of quasi CNQDs facilitate the charge transfer of ZIS/TCN, resulting in a slight enhancement in PL emission intensity of 2CNQDs/CZ40 compared with CZ40 [46]. In contrast, the PL emission intensity CZ40 as well as 2CNQDs/CZ40 are great suppressed due to the construction of S-scheme heterojunction and Schottky junction, revealing that electrons photoexcited from TCN can be effectively captured by $ZnIn_2S_4$ or CNQDs rather than directly taking part in the fluorescence emission. Such suppress process are also reflected by TRPL. As shown in Fig. 7b, the average PL lifetime (τ_{ave}) is fitted via the triple-exponential model (See **S2.2** in SI for detailed calculation), and the τ_{ave} of samples is recorded in Table S2. The τ_{ave} prolongs in the following order: TCN (8.69 ns) < CZ40 (10.56 ns) < 2CNQDs/CZ40 (11.5 ns). The longest τ_{ave} of 2CNQDs/CZ40 testifies the Schottky junction cooperates with S-scheme to accelerate interfacial charge separation and transfer kinetic, and maximizing the utilization
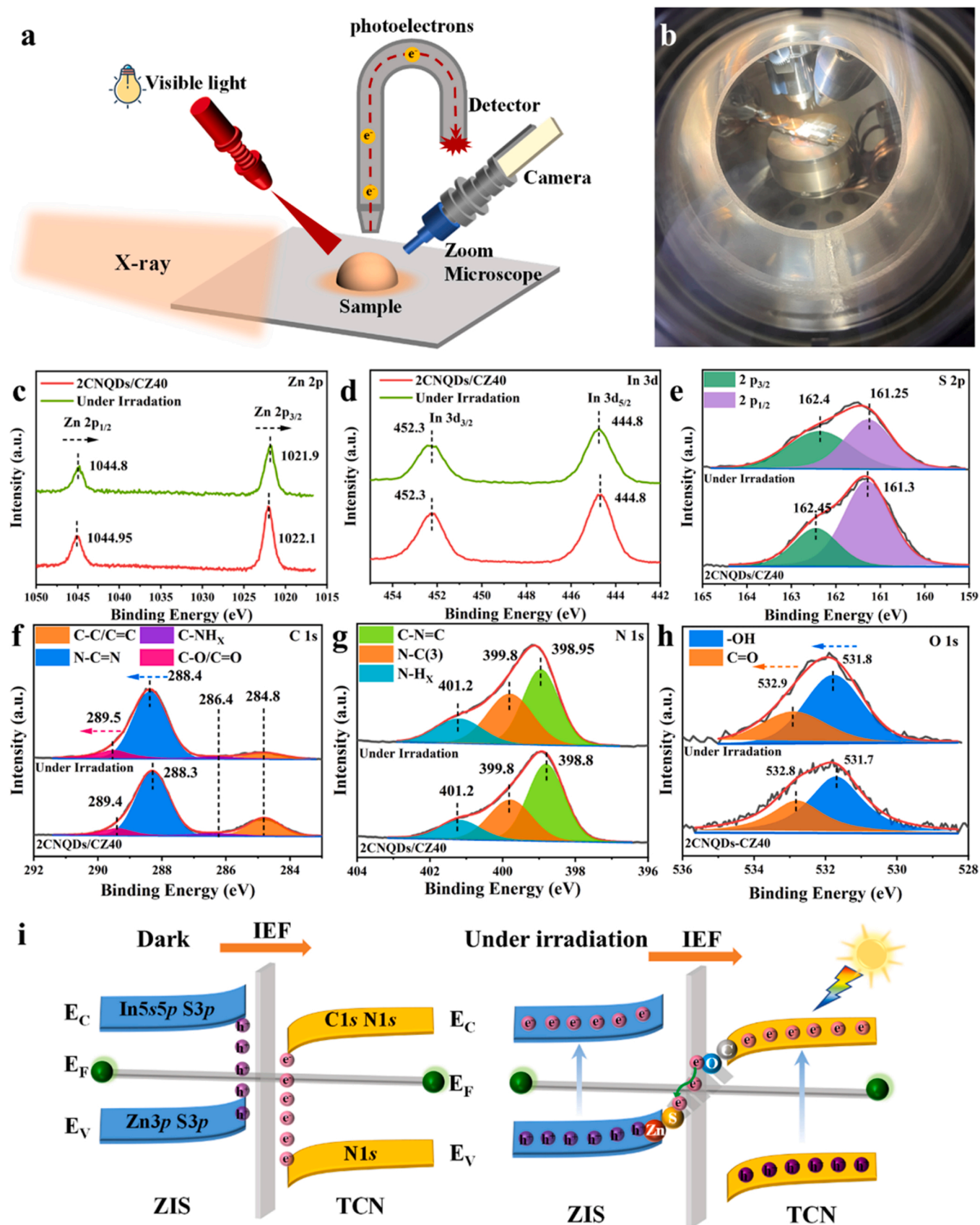
Fig. 6. (a) Schematic illustration and (b) Equipment illustration of synchronous illumination X-ray photoelectron spectroscopy; High-resolution SI-XPS (c) Zn 2p, (d) In 3d, (e) S 2p, (f) C 1s, (g) N 1s, (h) O 1s spectra of 2CNQDs/CZ40; (i) The electron transfer in the process of SI-XPS.
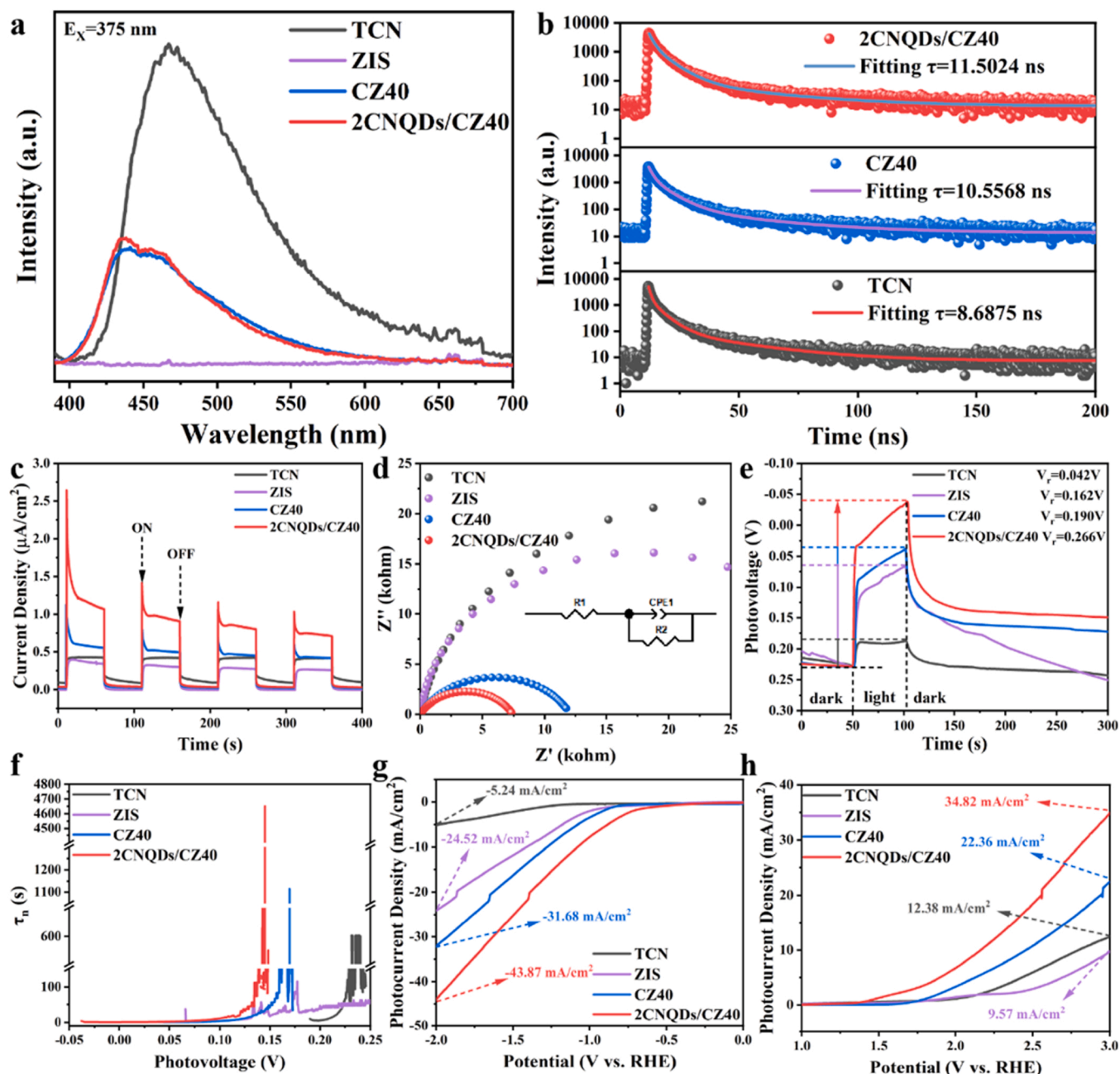
Fig. 7. (a) PL spectra and (b) TRPL spectra of samples; (c) Transient photocurrent response; (d) EIS Nyquist plots; (e) Open-circuit voltage; (f) Average photoelectron lifetime; (g) LSV with 0 V to − 2.0 V vs. RHE, (h) LSV with 0–3.0 V vs. RHE.

efficiency of carriers in the following surface photocatalytic reaction.

On the other hand, carriers' separation dynamics are either explored by photoelectrochemical technique. Transient photocurrent response (TPC) generally represents the degree of carrier' separation, the larger the photocurrent intensity, the easier the carrier separation. As shown in Fig. 7c, TPC intensity of 2CNQDs/CZ40 achieves 2.61 µA/cm^2, which is 7.46, 6.52 and 2.35 times larger than that of TCN (0.35 µA/cm^2), ZnIn$_2$S$_4$ (0.35 µA/cm^2) and CZ40 (0.35 µA/cm^2) (Fig. S12). The highest TPC density confirms superior photoinduced excitons' dissociation dynamics for 2CNQDs/CZ40. In addition, such properties are also testified by EIS tests (Fig. 7d and Table S3). The smaller the impedance semi-circular arc radius, the smaller charge migration resistance, and higher separation efficiency [47]. The EIS semicircular arc radius decreases in the following order: TCN > ZnIn$_2$S$_4$ > CZ40 > 2CNQDs/CZ40, which manifest the smallest electron transfer resistance of 2CNQDs/CZ40 and

corresponding the superior carriers' separation efficiency.

Open-circuit voltage decay (OCVD) curves are investigated to study the charge recombination process (Fig. 7e). The more efficient decay rate, the more enhanced charge separation efficiency. 2CNQDs/CZ40 exhibits the largest photovoltage decay rate (0.266 V) compared with other counterparts (0.042, 0.162 and 0.190 V for TCN, ZnIn$_2$S$_4$ and CZ40, respectively), which suggests simultaneous S-scheme and Schottky typed heterostructure facilitate the charge separation, thus resulting in considerable charge accumulation. In addition, the electron lifetime (τ_n) is calculated quantitatively by OVCD results (See S2.3 in SI for detailed calculation) [48]. As presented in Fig. 7f, the photoelectron of 2CNQDs/CZ40 could be transferred continuously for up to 4600 s, CZ40 could also operate for long period of 0–1100 s. All of their τ_n are prolonged compared to that of TCN (0–600 s) and ZIS (0–100 s), veri-fying that the synergy of S-scheme and Schottky structure is capable of

accelerating the charge separation and transfer. The linear sweep voltammetry (LSV) curves at diverse voltages are investigated to explore redox properties of samples. As exhibited in Fig. 7g, the photocurrent density of 2CNQDs/CZ40 achieves 43.87 mA/cm^2 at − 2.0 V (vs. RHE) compared with other counterparts (CZ40 (31.68 mA/cm^2) > ZnIn$_2$S$_4$ (24.52 mA/cm^2) > TCN (5.24 mA/cm^2) at same voltage, signification of superior reducibility of 2CNQDs/CZ40. Simultaneously, strong oxidation is either supported by LSV at 0–3.0 V vs. RHE shown in Fig. 7h, the photocurrent density of 2CNQDs/CZ40 reaches 34.82 mA/cm^2 compared to others CZ40 (22.36 mA/cm^2) > TCN (12.38 mA/cm^2) > ZnIn$_2$S$_4$ (9.57 mA/cm^2) at same voltage. Compared with the single component and two-component catalysts, the photoelectrochemical results demonstrate the superiority of the excellent spatial separation and transportation of photogenerated charges of 2CNQDs/CZ40 composites [49]. It highlights the cooperation of Schottky junction and S-scheme accelerate the carrier separation kinetics from different spatial interface regions.

3.2. Photocatalytic degradation performance for petroleum hydrocarbon

The photocatalytic degradation activity towards petroleum hydrocarbon in water (artificial seawater) are evaluated in lab-scale for photocatalysts. The control experiments are carried out to ensure the activity are attributed to photocatalyst without other interfere factor. The loss of C14 is negligible in photolysis or dark experiments (Figs. 8a and S13). TCN and ZnIn$_2$S$_4$ exhibits comparable activity under visible light illumination for 4 h (TCN (21.36%) and ZIS (19.59%)). Significantly, coupling TCN with ZnIn$_2$S$_4$ to construct S-scheme heterojunction contributes to the degradation activity of CZ catalysts, especially CZ40 achieves 38.1% under same conditions when the ZnIn$_2$S$_4$ weight ratio of 40%, which is the highest among binary samples. More importantly, the introduction of CNQDs to CZ40 propels the activity universally, the 2CNQDs/CZ40 exhibits highest photocatalytic removal efficiency of 58.48% when the decoration weight ratio is 2% (Fig. 8b). Such results highlight the advantages of the Schottky mechanism composed of CNQDs and individual semiconductors (TCN, ZnIn$_2$S$_4$). To be fair,
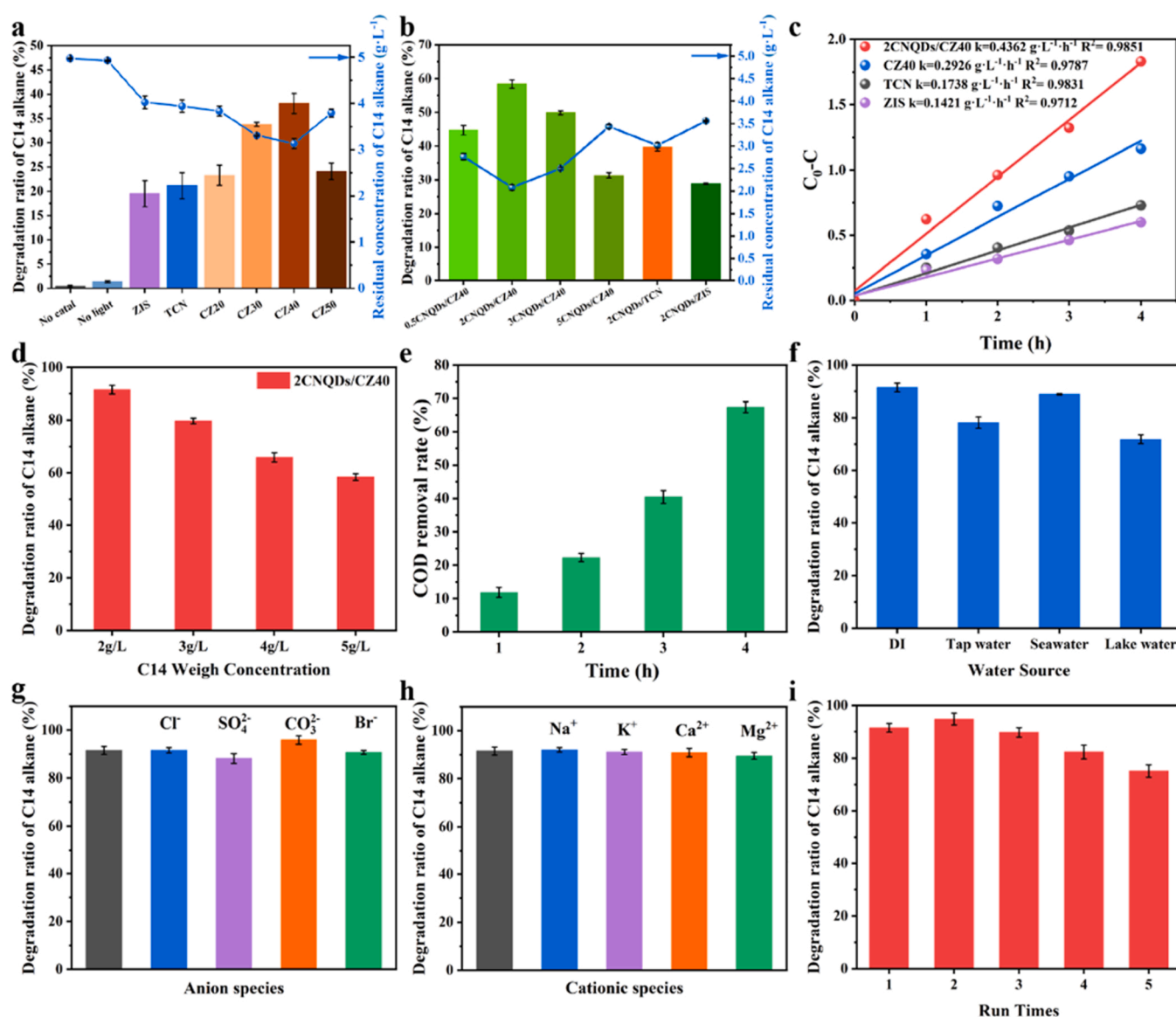

Fig. 8. (a) Photocatalytic activity for the removal of C14 and its residual concentration for TCN, ZIS and CZ series with 5 g/L C14; (b) Photocatalytic activity for the removal of C14 and its residual concentration for 2CNQDs/TCN, 2CNQDs/ZIS and CNQDs/CZ40 series with 5 g/L C14; (c) Corresponding reaction kinetics of samples with 2 g/L C14; (d) Effect of weight concentration of C14; (e) COD removal rate over 2CNQDs/CZ40 with 2 g/L C14; Effects of (f) Water source, (g) Coexisting anion species and (h) Coexisting cationic species on the removal of C14 with 2 g/L C14. (i) Cycling stability of 2CNQDs/CZ40 for C14 removal with 2 g/L C14.

although the single Schottky junction of CNQDs/TCN and CNQDs/ZnIn$_2$S$_4$ shows enhanced activity compared to their counterpart (CNQDs/TCN 40.69% and CNQDs/ZnIn$_2$S$_4$ 28.91%), they are still inferior to that of 2CNQDs/CZ40 where S-scheme and Schottky-scheme synergize mutually. The reaction kinetics are investigated according to different reaction model. It is found the photocatalytic degradation kinetics is most relevant to zero-order reactions (Table S4). Hence, the apparent reaction rate constants (k) are fitted shown in Fig. 8c, the k values of 2CNQDs/CZ40, CZ40, TCN and ZnIn$_2$S$_4$ are calculated to be 0.4362, 0.2926, 0.1738 and 0.1421 g L^{-1} h^{-1}, respectively. Apparently, the 2CNQDs/CZ40 possesses the largest k value (0.4362 g L^{-1} h^{-1}), which is 1.49, 2.51 and 3.1-fold higher than that of CZ40, TCN and ZnIn$_2$S$_4$. The effect of C14 concentration on the performance are studied as shown in Fig. 8d, the catalytic activity of optimal 2CNQDs/CZ40 increases with decrease of C14 concentration from 5 g/L to 2 g/L, specifically photocatalytic performance of 2CNQDs/CZ40 increases to 91.5% with 2 g/L C14 than that with 5 g/L C14 (58.48%), and the results over other samples are shown in Fig. S14. It is noteworthy that it is rather comparable performance compared with other previous reports (Table S5).

Chemical Oxygen Demand (COD) is a crucial parameter for evaluating the removal efficiency of organic pollutants in water [50]. The actual removal efficiency of 2CNQDs/CZ40 for n-tetradecane in water is illustrated in Fig. 8e. The COD of the untreated wastewater with 2 g/L n-tetradecane was 361.21 mg/L, and 67.37% of COD is significantly reduced through 4 h photocatalytic process. It implies the 2CNQDs/CZ40 photocatalyst will be an alterative environmental functional material to remove alkanes in water efficiently.

Aiming to remediate water area polluted by oil spill in real world, effect of the reaction parameters including water quality and ions on the C14 removal efficiency are investigated. As shown in Fig. 8f, photocatalytic degradation efficiency is still as high as 88.87% in artificial seawater, indicating that the anions and cations in seawater have almost no effect on the photocatalytic degradation mechanism of C14. Tap water and lake water have obvious inhibition (Tap water (78.15%); lake water (71.87%)), which may be caused by the presence of microorganism and abundant humic acid [51]. These species compete to consume active free radicals, resulting in the decrease of catalytic degradation performance. In consideration of various ions in marine environment, the influence of various cations and anions on the catalytic activity are evaluated as shown in Fig. 8g and h. All of ion concentration is adjusted to 1 mM. For anions, the halogen ions such as Cl$^-$ and Br$^-$ have little effect on the degradation efficiency. Nevertheless, the SO$_4^{2-}$ could capture active radicals •OH produced by light excitation of 2CNQDs/CZ40, thus reducing the photocatalytic activity [52]. On the contrary, the addition of carbonate provides a weak alkaline environment for the degradation process. The increase in the number of OH$^-$ enhances the number of hydroxyl radicals formed by the oxidation of OH$^-$ via photogenerated holes, thus promoting the hydroxyl radicals to participate in the reaction path of C14 catalytic degradation. For cations, both monovalent (Na$^+$, K$^+$) and divalent ions (Ca^{2+}, Mg^{2+}) have little effect on the reaction performance (Fig. 8h).

Last but not least, recycle stability of the optimal 2CNQDs/CZ40 photocatalyst are evaluated. Through the secondary extraction process, the residual C14 was not detected in the recirculated 2CNQDs/CZ40 (Fig. S13). As shown in Fig. 8i, as high as 75.2% of degradation efficiency is retained after 5 successive recycle runs. The further characterization implies the bulk structure as well as surface functional group remains the same as those of fresh one although micro-morphology tends to aggregates (Fig. S15). It indicates the superior recycle stability of 2CNQDs/CZ40 photocatalyst.

3.3. Possible photocatalytic reaction pathways and mechanisms

Sacrificial agent experiments are carried out to explore the roles of reactive radicals generated by 2CNQDs/CZ40 with TBA, p-BQ (1,4-Benzoquinone) and EDTA-2Na as scavengers of hydroxyl radicals (•OH), superoxide radicals (•O$_2^-$) and holes (h$^+$), respectively. As shown in Fig. 9a, the addition of EDAT-2Na and TBA have some effect on the catalytic efficiency for pristine TCN, which merely achieves 64.7% and 89.4% of original activity. Such results are well matched with the energy level structure of TCN, VB of TCN contributed to the formation of h$^+$ and •OH, while superoxide radicals (•O$_2^-$) is hardly generated because of insufficient redox ability or much negative of CB potential. The superoxide radicals (•O$_2^-$) and holes (h$^+$) have some inhibited impact on the catalytic activity for pristine ZnIn$_2$S$_4$, which is either consistent with the E$_{CB}$ and E$_{VB}$ potentials (Fig. 3e). Noted VB of ZnIn$_2$S$_4$ cannot oxidize OH$^-$ to produce hydroxy radicals •OH due to its much negative VB position shown in Fig. 3e. It is assumed that only •OH, •O$_2^-$ and h$^+$ could oxidize C14 in the photocatalytic system, therefore the contribution of each reactive species to photocatalytic degradation of C14 is calculated by trapping experiment (See S2.4 in SI for detailed calculation). As shown in Fig. 9b, the h$^+$ contributes 71.13% and 52% of degradation efficiency for TCN and ZnIn$_2$S$_4$ respectively, which is predominant reactive radicals in their respective systems.

Significantly, TBA, p-BQ and EDAT-2Na all have obvious negative effect on the catalytic performance for CZ40, which implies abundant •OH, •O$_2^-$ and h$^+$ are produced during visible light illumination. Among them TBA suppresses activity the best (Loss 34% of degradation rate), p-BQ middle and EDAT-2Na third. It is well explained by its S-scheme energy level of CZ40 shown in Fig. 3e, much stronger redox ability is obtained for S-scheme heterojunction compared to sole semiconductors (TCN and ZnIn$_2$S$_4$). The reactive radicals transform from h$^+$ in sole TCN or ZnIn$_2$S$_4$ to •OH in CZ40, highlighting the stronger oxidation ability of VB of TCN in S-scheme CZ40. Correspondingly, as shown in Fig. 9b, the •OH contributes more than 58% towards C14 degradation for CZ40, then •O$_2^-$ (24.17%) and h$^+$ (18.05%). It indicates the role of h$^+$ is greatly weakened, while the role of •OH as well as •O$_2^-$ is greatly enhanced compared to pristine TCN and ZnIn$_2$S$_4$. Such phenomenon is enlarged further for 2CNQDs/CZ40 compared to the above discussed CZ40, especially the contribution of •O$_2^-$ are largely enhanced due to the Schottky synergy of CNQDs with TCN and ZnIn$_2$S$_4$. It is worth noting that the contribution of •OH, •O$_2^-$ and h$^+$ achieves 44.17%, 33.46% and 22.37% respectively in 2CNQDs/CZ40 system, and each one is larger than that of the corresponding CZ40 catalyst (Fig. 9b). The optimization of the type and number of free radicals confirms the advantages of the cooperative CNQDs Schottky junction with S-scheme heterojunction compared to solo S-scheme heterojunction. It implies 0D/2D/2D S-S strategy can optimize the separation and transport of photogenerated carriers effectively everywhere in material, thus better utilizing the redox properties of the energy band structure of materials, and eventually exhibiting excellent photocatalytic performance for photocatalytic removal of alkane.

In depth, in-situ ESR techniques are employed to explore the quantitative information of reactive radicals as shown in Fig. 9 c-j. The DMPO agents are utilized as scavenger to generate paramagnetic adduct with •OH as well as •O$_2^-$ in water and methanol solution, respectively. At the same scale, it is obvious 2CNQDs/CZ40 exhibits the strongest peaks of •OH adduct with characteristic intensity of 1:2:2:1 after visible light illumination for 10 min compared to that of CZ40 and pristine TCN. The peak intensity information of characteristic •OH signals is sorted as follows: 2CNQDs/CZ40 > CZ40 > TCN. It is solely ascribed to the photochemical process because there are not signals in the dark conditions for all photocatalysts. Clearly, as shown in Fig. S17, because the •OH peak intensity of 2CNQDs/CZ40 in N$_2$ atmosphere was almost the same as that in environmental condition, the all •OH were attributed to the oxidation of H$_2$O or OH$^-$ species by the photogenerated holes on TCN (2.49 eV vs. NHE; E [H$_2$O/•OH] = 2.40 eV vs. NHE), verifying the construction of S-scheme rather than type II heterojunction. It testifies the sufficient oxidation capacity of 2CNQDs/CZ40 and its optimized band alignment contributes to separation as well as transfer of photoexcited carriers, being conducive to production of strong oxidized
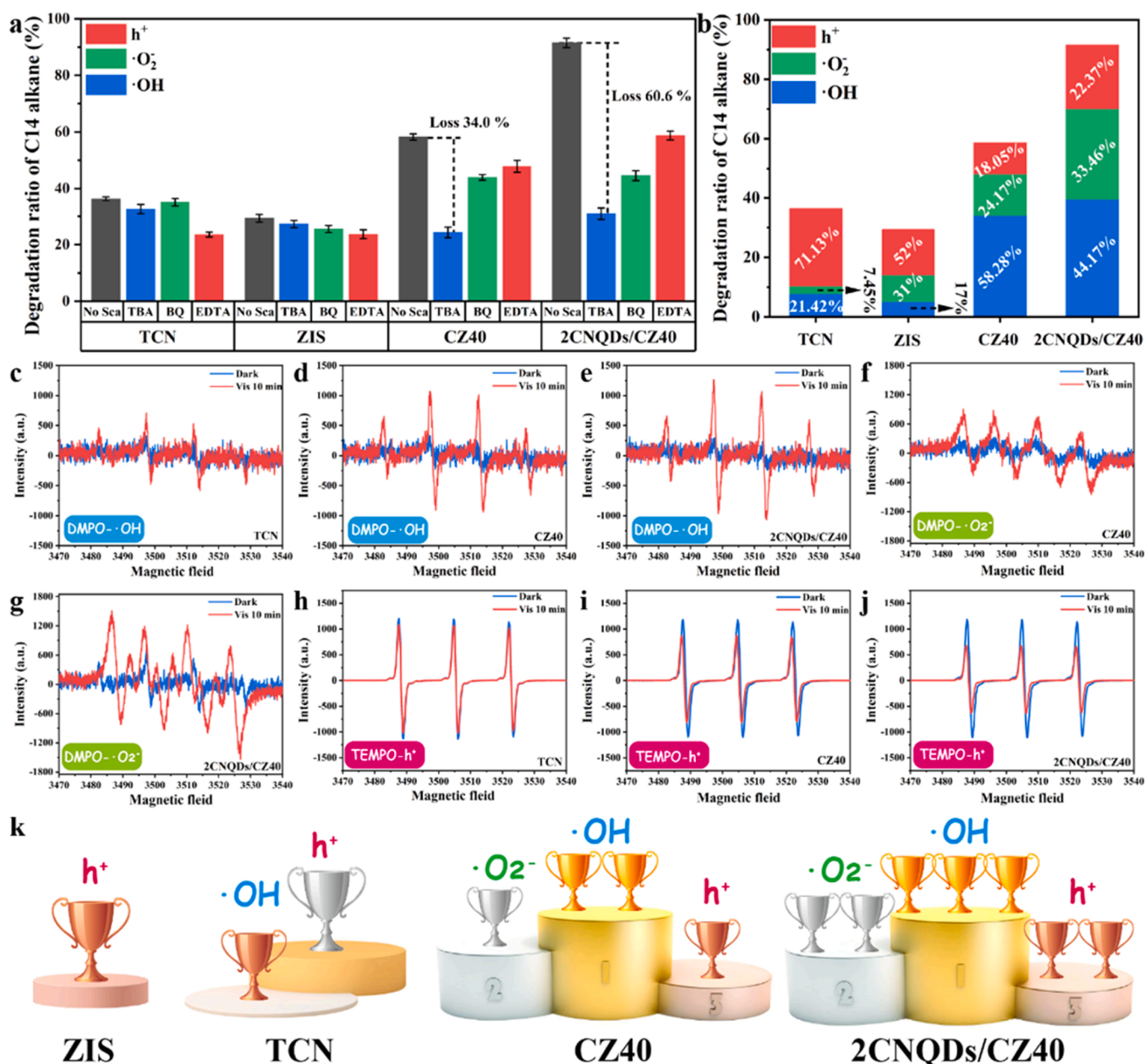
Fig. 9. (a) Photocatalytic degradation of C14 with different scavengers over samples; (b) Contribution of active radicals to the degradation of C14, assuming that only ●OH, ●O$_2^-$ and h$^+$ in the system; (c-j) In-situ ESR spectra of samples were studied via using DMPO and TEMPO to quench active radicals; (k) The validation results for ESR and trapping experiments.

hydroxyl radicals ●OH. The concentration or peak intensity of ●O$_2^-$ of 2CNQDs/CZ40 is either stronger than that of CZ40 from ESR results shown in Fig. 9f and g, which highlight the crucial roles of CNQDs towards the carriers' separation kinetics. Interestingly, it is also found that 2CNQDs/CZ40 either exhibits characteristic peak of ●O$_2^-$ in the absence of light excitation, which may be because the CNQDs with large work function tend to accumulate electrons from other semiconductors, facilitating the generation of ●O$_2^-$ by single electron reduction of molecular oxygen. Correspondingly, the catalytic degradation activity of 2CNQDs/CZ40 catalyst towards C14 in water achieves 14.0% under dark condition without external energy driven (Fig. S16). The TEMPO agents are used as scavenger to generate paramagnetic adduct with h$^+$ in water solution. As shown in Fig. 9h-j, the h$^+$ concentration decreases as follows order: 2CNQDs/CZ40 > CZ40 > TCN. The amount of h$^+$ is largest for 2CNQDs/CZ40 composites, testifying the effectiveness of the synergy effect of Schottky junction with S-scheme heterojunction in

suppressing recombination of photogenerated electron and hole pairs anywhere [53]. To sum up, significantly ●OH, ●O$_2^-$ and h$^+$ all play predominant roles in catalytic reaction for 2CNQDs/CZ40 system compared to either binary CZ40 or single semiconductor (TCN, ZnIn$_2$S$_4$), more importantly, the number of reactive radicals is also the most among all the catalysts. Such advantages are mainly ascribed to the contribution of Schottky junction and S-scheme illustrated in Fig. 9k.

GC-MS technique is employed to confirm the intermediates during the photocatalytic reaction shown in Figs. S18–S26. The degradation path is proposed in combination with the reaction free radicals discussed above, we try to propose such a degradation path as follows. 2CNQDs/CZ40 photocatalyst is excited by visible light to generate corresponding free radicals, which attack n-tetradecane to remove one carbon atom from C14 to form C13 product (Eqs. (1)–(11)), and so on to complete the entire catalytic degradation path. As illustrated in Fig. 10a, ●OH, h$^+$ and ●O$_2^-$ play predominant roles in photocatalytic oxidation of alkanes in this
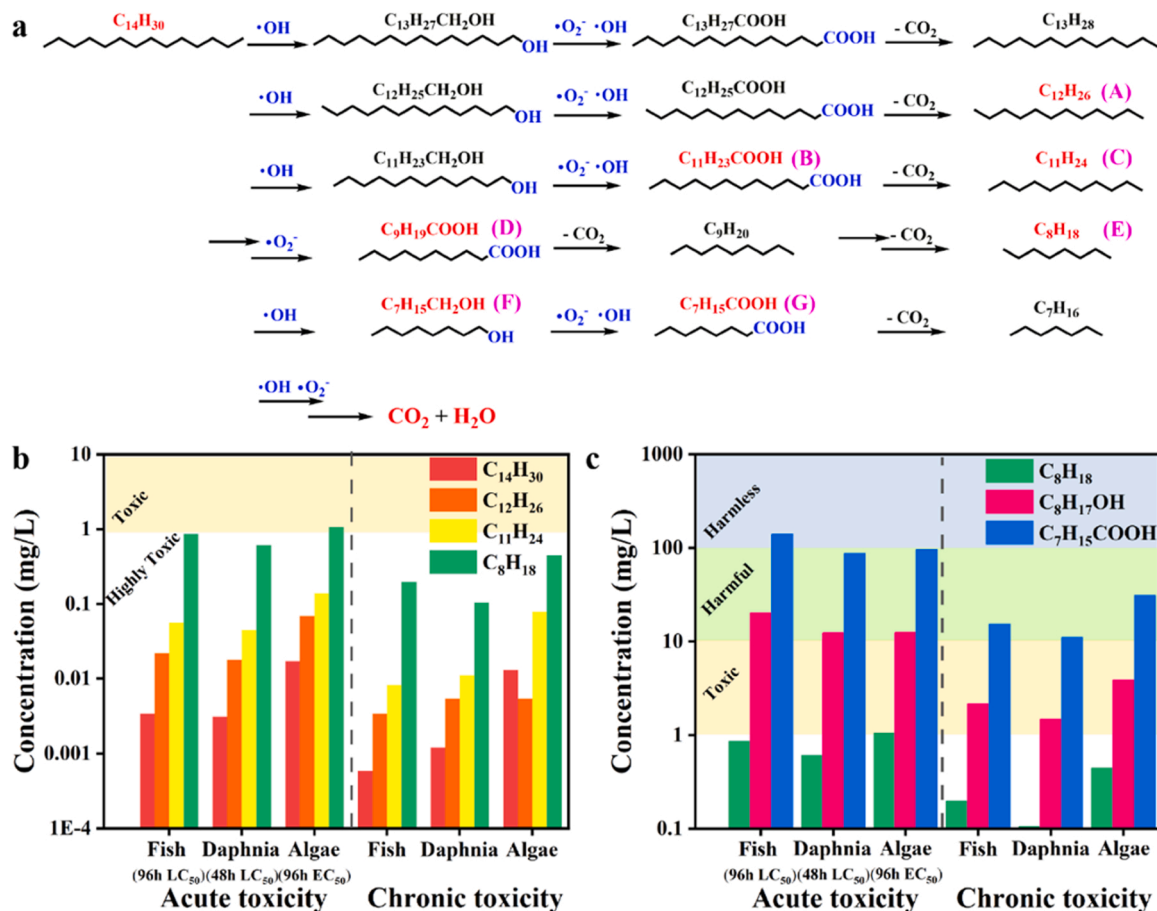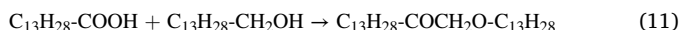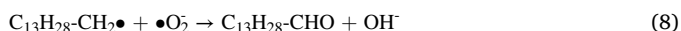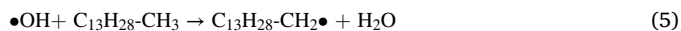
Fig. 10. (a) Proposed reaction mechanism for C14 degradation over 2CNQDs/CZ40; (b) Toxicity evaluation of C14 and degradation alkanes (C12, C11 and C8) for fish, daphnia and green algae over 2CNQDs/CZ40 (LC$_{50}$ represents the half lethal concentration and EC$_{50}$ represents the half effective concentration); (c) Toxicity evaluation of C8, derived alcohol and acid for fish, daphnia and green algae over 2CNQDs/CZ40.

reaction system. The alkanes are attacked by •OH to form carbon radicals, which are converted to corresponding short-chain alcohol, aldehyde and carboxylic acid, such as $C_8H_{17}OH$ (F), $C_{11}H_{23}COOH$ (B), $C_9H_{19}COOH$ (D) and $C_7H_{15}COOH$ (G). The short-chain alkane is then generated by Photo-Kolbe reaction of carboxylic acid like $C_{12}H_{26}$ (A), $C_{11}H_{24}$ (C) and C_8H_{18} (E) [54–56]. Thus, long-chain alkane is cut short step by step to produce short- chain alkane, which were oxidized finally to CO_2 and H_2O by the reaction with reactive •OH and •O_2^- radicals.

$$P + h\nu \rightarrow e^- + h^+ \tag{1}$$

$$e^- + O_2 \rightarrow \bullet O_2^- \tag{2}$$

$$h^+ + H_2O/OH^- \rightarrow \bullet OH \tag{3}$$

$$h^+ + C_{13}H_{28}\text{-}CH_3 \rightarrow C_{13}H_{28}\text{-}CH_2\bullet \tag{4}$$

$$\bullet OH + C_{13}H_{28}\text{-}CH_3 \rightarrow C_{13}H_{28}\text{-}CH_2\bullet + H_2O \tag{5}$$

$$C_{13}H_{28}\text{-}CH_2\bullet + \bullet OH \rightarrow C_{13}H_{28}\text{-}CH_2OH \tag{6}$$

$$C_{13}H_{28}\text{-}CH_2OH + \bullet OH \rightarrow C_{13}H_{28}\text{-}CHO + H_2O \tag{7}$$

$$C_{13}H_{28}\text{-}CH_2\bullet + \bullet O_2^- \rightarrow C_{13}H_{28}\text{-}CHO + OH^- \tag{8}$$

$$C_{13}H_{28}\text{-}CHO + \bullet OH \rightarrow C_{13}H_{28}\text{-}COOH \tag{9}$$

$$C_{13}H_{28}\text{-}COOH + \bullet O_2^- \rightarrow C_{13}H_{28} + CO_2 \tag{10}$$

$$C_{13}H_{28}\text{-}COOH + C_{13}H_{28}\text{-}CH_2OH \rightarrow C_{13}H_{28}\text{-}COCH_2O\text{-}C_{13}H_{28} \tag{11}$$

In addition to catalytic performance of removing alkane rapidly and effectively, marine eco-environments should not be disturbed in

principle by the application of treatment technology whether physical, chemical and biological methods [57]. Hence, the toxicity of intermediates during the reaction are evaluated by Ecological Structure Activity Relationships (ECOSAR) program proposed by US. EPA. The acute and chronic toxicity for fish, daphnia and green algae are indexed shown in Fig. 10b, c and Table S6. It is obvious that the parent $C_{14}H_{30}$ was "Highly Toxic" for marine organism, with the reaction goes on the short-chain alkanes ($C_{12}H_{26}$ (A), $C_{11}H_{24}$ (C) and C_8H_{18} (E)) exhibits weak acute and chronic toxicity compared with its parent, especially the acute toxicity of C_8H_{18} of 96-h algae EC$_{50}$ was 1.06 mg/L, whose toxicity evaluation demotes to "Toxic". More meaningful, some intermediates like alcohol and carboxylic acid exhibit much weaker toxicity ($C_8H_{17}OH$ (F), $C_{11}H_{23}COOH$ (B), $C_9H_{19}COOH$ (D) and $C_7H_{15}COOH$ (G)). For example, the acute and chronic toxicity of $C_7H_{15}COOH$ demotes to "Harmful" or even "Harmless", which indicate photocatalytic degradation reaction of C14 over 2CNQDs/CZ40 have not negative toxic effects on water eco-environments, or conservatively, whose toxicity are not larger than that of parent alkanes.

4. Conclusion

In conclusion, Schottky junction relying on 0D materials synergies with 2D/2D S-scheme heterojunction strategy (S-S strategy) were proposed to overcome the problem that carriers cannot be separated efficiently uniformly in 2D/2D S-scheme heterojunction in real circumstance. Series of CNQDs/TCN/ZnIn$_2$S$_4$ was synthesized by facile one-pot solvothermal method. Kelvin probe force microscopy (KPFM) and Synchronous irradiation XPS (SI-XPS) confirmed the resulted strong

interfacial electronic field induce by the introduction of CNQDs with large work function. Photoluminescence (Steady-State PL, transient-state PL) and Photoelectrochemical experiments testified the highly efficient of photoinduced carriers' separation behavior anywhere. Such two aspects are conducive to the production of reactive radicals in water or seawater by ternary photocatalysts both for type and quantity of radicals. The CNQDs/TCN/ZnIn$_2$S$_4$ demonstrates the best performance towards catalytic degradation of n-tetradecane in seawater in all conditions. The $\bullet$OH, h$^+$ and $\bullet$O$_2^-$ plays predominant roles in photocatalytic oxidation of alkanes in this reaction system. Reaction factor including water quality, anions and cations were also investigated aiming for application in practical conditions. Simultaneously, recycle stability, reaction mechanism, reaction path and eco-toxicity were also systematically investigated. Finally, it is proved Schottky junction relying on 0D materials cooperates with 2D/2D S-scheme junction may be an effective strategy for uniform separation of photoinduced carriers in S-scheme heterojunction at every contacting point, and the resulted CNQDs/TCN/ZnIn$_2$S$_4$ heterostructure with this idea will be a promising candidate for "green" elimination of oil spill.

CRediT authorship contribution statement

Linhong Xia: Data curation, Formal analysis, Writing – original draft. **Kaisheng Zhang**: Resources, Methodology, Writing – review & editing. **Xudong Wang:** Investigation, Writing – review & editing. **Qi Guo:** Formal analysis, Writing – review & editing. **Yuning Wu:** Data curation, Formal analysis. **Yujie Du:** Data curation, Writing – review & editing. **Lixue Zhang:** Resources, Writing – review & editing. **Jianfei Xia:** Resources, Writing – review & editing. **Hua Tang:** Writing – review & editing. **Xia Zhang:** Resources, Writing – review & editing. **Yanhua Peng**: Formal analysis, Writing – review & editing. **Zhuo Li:** Methodology, Formal analysis, Writing – review & editing. **Xiaolong Yang**: Conceptualization, Methodology, Formal analysis, Funding acquisition, Supervision, Writing – review & editing.

Declaration of Competing Interest

The authors declare that they have no known competing financial interests or personal relationships that could have appeared to influence the work reported in this paper.

Data availability

Data will be made available on request.

Acknowledgments

Appendix A. Supplementary material

Supplementary data associated with this article can be found in the online version at doi:10.1016/j.apcatb.2023.122387.

References

[1] Z. Wan, J. Chen, Human errors are behind most oil-tanker spills, Nature 560 (2018) 161–163, https://doi.org/10.1038/d41586-018-05852-0.

[2] X. Yang, H. Sun, G. Li, T. An, W. Choi, Fouling of TiO$_2$ induced by natural organic matters during photocatalytic water treatment: mechanisms and regeneration strategy, Appl. Catal. B Environ. 294 (2021), 120252, https://doi.org/10.1016/j.apcatb.2021.120252.

[3] W.-J. Ong, L.-L. Tan, Y.H. Ng, S.-T. Yong, S.-P. Chai, Graphitic carbon nitride (g-C$_3$N$_4$)-based photocatalysts for artificial photosynthesis and environmental remediation: are we a step closer to achieving sustainability, Chem. Rev. 116 (2016) 7159–7329, https://doi.org/10.1021/acs.chemrev.6b00075.

[4] V. Hasija, V.-H. Nguyen, A. Kumar, P. Raizada, V. Krishnan, A.A.P. Khan, P. Singh, E. Lichtfouse, C. Wang, P. Thi Huong, Advanced activation of persulfate by polymeric g-C$_3$N$_4$ based photocatalysts for environmental remediation: a review, J. Hazard. Mater. 413 (2021), 125324, https://doi.org/10.1016/j.jhazmat.2021.125324.

[5] V. Hasija, P. Raizada, A. Sudhaik, K. Sharma, A. Kumar, P. Singh, S. B. Jonnalagadda, V.K. Thakur, Recent advances in noble metal free doped graphitic carbon nitride based nanohybrids for photocatalysis of organic contaminants in water: a review, Appl. Mater. Today 15 (2019) 494–524, https://doi.org/10.1016/j.apmt.2019.04.003.

[6] L. Xia, Z. Sun, Y. Wu, X.-F. Yu, J. Cheng, K. Zhang, S. Sarina, H.-Y. Zhu, H. Weerathunga, L. Zhang, J. Xia, J. Yu, X. Yang, Leveraging doping and defect engineering to modulate exciton dissociation in graphitic carbon nitride for photocatalytic elimination of marine oil spill, Chem. Eng. J. 439 (2022), 135668, https://doi.org/10.1016/j.cej.2022.135668.

[7] Q. Guo, Y. Wu, L. Xia, X.-F. Yu, K. Zhang, Y. Du, L. Zhang, H. Tang, J. Cheng, J. Shang, Y. Peng, Z. Li, X. Man, X. Yang, Stitching electron localized heptazine units with "carbon patches" to regulate exciton dissociation behavior of carbon nitride for photocatalytic elimination of petroleum hydrocarbons, Chem. Eng. J. (2022), 139092, https://doi.org/10.1016/j.cej.2022.139092.

[8] J. Wang, S. Wang, A critical review on graphitic carbon nitride (g-C$_3$N$_4$)-based materials: preparation, modification and environmental application, Coord. Chem. Rev. 453 (2022), 214338, https://doi.org/10.1016/j.ccr.2021.214338.

[9] X. Yu, S.-F. Ng, L.K. Putri, L.-L. Tan, A.R. Mohamed, W.-J. Ong, Point-defect engineering: leveraging imperfections in graphitic carbon nitride (g-C$_3$N$_4$) photocatalysts toward artificial photosynthesis, Small (2021) 2006851, https://doi.org/10.1002/smll.202006851.

[10] A. Kumar, P. Raizada, A. Hosseini-Bandegharaei, V.K. Thakur, V.-H. Nguyen, P. Singh, C-, N-vacancy defect engineered polymeric carbon nitride towards photocatalysis: viewpoints and challenges, J. Mater. Chem. A 9 (2021) 111–153, https://doi.org/10.1039/D0TA08384D.

[11] Q. Xu, L. Zhang, B. Cheng, J. Fan, J. Yu, S-scheme heterojunction photocatalyst, Chem 6 (2020) 1543–1559, https://doi.org/10.1016/j.chempr.2020.06.010.

[12] F.A. Qaraah, S.A. Mahyoub, A. Hezam, A. Qaraah, F. Xin, G. Xiu, Synergistic effect of hierarchical structure and S-scheme heterojunction over O-doped g-C$_3$N$_4$/N-doped Nb$_2$O$_5$ for highly efficient photocatalytic CO$_2$ reduction, Appl. Catal. B Environ. 315 (2022), 121585, https://doi.org/10.1016/j.apcatb.2022.121585.

[13] P. Xia, S. Cao, B. Zhu, M. Liu, M. Shi, J. Yu, Y. Zhang, Designing a 0D/2D S-scheme heterojunction over polymeric carbon nitride for visible-light photocatalytic inactivation of bacteria, Angew. Chem. Int. Ed. 59 (2020) 5218–5225, https://doi.org/10.1002/anie.201916012.

[14] J. Fu, Q. Xu, J. Low, C. Jiang, J. Yu, Ultrathin 2D/2D WO$_3$/g-C$_3$N$_4$ step-scheme H$_2$-production photocatalyst, Appl. Catal. B Environ. 243 (2019) 556–565, https://doi.org/10.1016/j.apcatb.2018.11.011.

[15] L. Li, D. Ma, Q. Xu, S. Huang, Constructing hierarchical ZnIn$_2$S$_4$/g-C$_3$N$_4$ S-scheme heterojunction for boosted CO$_2$ photoreduction performance, Chem. Eng. J. 437 (2022), 135153, https://doi.org/10.1016/j.cej.2022.135153.

[16] V.B.Y. Oh, S.F. Ng, W.J. Ong, Shining light on ZnIn2S4 photocatalysts: promotional effects of surface and heterostructure engineering toward artificial photosynthesis, EcoMat (2022), https://doi.org/10.1002/eom2.12204.

[17] M. Tan, Y. Ma, C. Yu, Q. Luan, J. Li, C. Liu, W. Dong, Y. Su, L. Qiao, L. Gao, Q. Lu, Y. Bai, Boosting photocatalytic hydrogen production via interfacial engineering on 2D ultrathin Z-scheme ZnIn$_2$S$_4$/g-C$_3$N$_4$ heterojunction, Adv. Funct. Mater. 32 (2022) 2111740, https://doi.org/10.1002/adfm.202111740.

[18] X. Deng, D. Wang, H. Li, W. Jiang, T. Zhou, Y. Wen, B. Yu, G. Che, L. Wang, Boosting interfacial charge separation and photocatalytic activity of 2D/2D g-C$_3$N$_4$/ZnIn$_2$S$_4$ S-scheme heterojunction under visible light irradiation, J. Alloy. Compd. 894 (2022), 162200, https://doi.org/10.1016/j.jallcom.2021.162209.

[19] Z. Wang, B. Cheng, L. Zhang, J. Yu, Y. Li, S. Wageh, A.A. Al-Ghamdi, S-Scheme 2D/2D Bi$_2$MoO$_6$/BiOI van der Waals heterojunction for CO$_2$ photoreduction, Chin. J. Catal. 43 (2022) 1657–1666, https://doi.org/10.1016/S1872-2067(21)64010-X.

[20] X. Yue, L. Cheng, J. Fan, Q. Xiang, 2D/2D BiVO$_4$/CsPbBr$_3$ S-scheme heterojunction for photocatalytic CO$_2$ reduction: Insights into structure regulation and Fermi level modulation, Appl. Catal. B Environ. 304 (2022) 120979, https://doi.org/10.1016/j.apcatb.2021.120979.

[21] J. Wang, Y. Yu, J. Cui, X. Li, Y. Zhang, C. Wang, X. Yu, J. Ye, Defective g-C$_3$N$_4$/covalent organic framework van der Waals heterojunction toward highly efficient S-scheme CO$_2$ photoreduction, Appl. Catal. B Environ. 301 (2022), 120814, https://doi.org/10.1016/j.apcatb.2021.120814.

[22] F. He, A. Meng, B. Cheng, W. Ho, J. Yu, Enhanced photocatalytic H$_2$-production activity of WO$_3$/TiO$_2$ step-scheme heterojunction by graphene modification, Chin. J. Catal. 41 (2020) 9–20, https://doi.org/10.1016/S1872-2067(19)63382-6.

[23] M.K. Bhunia, K. Yamauchi, K. Takanabe, Harvesting solar light with crystalline carbon nitrides for efficient photocatalytic hydrogen evolution, Angew. Chem. Int. Ed. 53 (2014) 11001–11005, https://doi.org/10.1002/anie.201405161.

[24] Z. Zeng, H. Yu, X. Quan, S. Chen, S. Zhang, Structuring phase junction between tri-s-triazine and triazine crystalline C_3N_4 for efficient photocatalytic hydrogen evolution, Appl. Catal. B Environ. 227 (2018) 153–160, https://doi.org/10.1016/j.apcatb.2018.01.023.

[25] Y. Pan, X. Hu, D. Shen, Z. Li, R. Chen, Y. Li, J. Lu, M. Bao, Facile construction of Z-scheme Fe-MOF@BiOBr/M−CN heterojunction for efficient degradation of ciprofloxacin, Sep. Purif. Technol. 295 (2022), 121216, https://doi.org/10.1016/j.seppur.2022.121216.

[26] N. Lu, X. Jing, J. Zhang, P. Zhang, Q. Qiao, Z. Zhang, Photo-assisted self-assembly synthesis of all 2D-layered heterojunction photocatalysts with long-range spatial separation of charge-carriers toward photocatalytic redox reactions, Chem. Eng. J. 431 (2022), 134001, https://doi.org/10.1016/j.cej.2021.134001.

[27] K. Schwinghammer, M.B. Mesch, V. Duppel, C. Ziegler, J. Senker, B.V. Lotsch, Crystalline carbon nitride nanosheets for improved visible-light hydrogen evolution, J. Am. Chem. Soc. 136 (2014) 1730–1733, https://doi.org/10.1021/ja411321s.

[28] Z. Xing, K. Dong, N. Pavlopoulos, Y. Chen, L. Amirav, Photoinduced self-assembly of carbon nitride quantum dots, Angew. Chem. Int. Ed. 60 (2021) 19413–19418, https://doi.org/10.1002/anie.202107079.

[29] Y. Li, M. Gu, T. Shi, W. Cui, X. Zhang, F. Dong, J. Cheng, J. Fan, K. Lv, Carbon vacancy in C_3N_4 nanotube: electronic structure, photocatalysis mechanism and highly enhanced activity, Appl. Catal. B Environ. 262 (2020), 118281, https://doi.org/10.1016/j.apcatb.2019.118281.

[30] S. Wang, B.Y. Guan, X.W.D. Lou, Construction of $ZnIn_2S_4$–In_2O_3 hierarchical tubular heterostructures for efficient CO_2 photoreduction, J. Am. Chem. Soc. 140 (2018) 5037–5040, https://doi.org/10.1021/jacs.8b02200.

[31] G. Dong, X. Huang, Y. Bi, Anchoring black phosphorus quantum dots on Fe-doped $W_{18}O_{49}$ nanowires for efficient photocatalytic nitrogen fixation, Angew. Chem. Int. Ed. 61 (2022), e202204271, https://doi.org/10.1002/anie.202204271.

[32] Y. Liu, J. Wu, F. Wang, Dibenzothiophene-S,S-dioxide-containing conjugated polymer with hydrogen evolution rate up to 147 mmol g^{-1} h^{-1}, Appl. Catal. B Environ. 307 (2022), 121144, https://doi.org/10.1016/j.apcatb.2022.121144.

[33] D. Zhao, C.-L. Dong, B. Wang, C. Chen, Y.-C. Huang, Z. Diao, S. Li, L. Guo, S. Shen, Synergy of dopants and defects in graphitic carbon nitride with exceptionally modulated band structures for efficient photocatalytic oxygen evolution, Adv. Mater. 31 (2019) 1903545, https://doi.org/10.1002/adma.201903545.

[34] Z. Miao, Q. Wang, Y. Zhang, L. Meng, X. Wang, In situ construction of S-scheme AgBr/BiOBr heterojunction with surface oxygen vacancy for boosting photocatalytic CO_2 reduction with H_2O, Appl. Catal. B Environ. 301 (2022), 120802, https://doi.org/10.1016/j.apcatb.2021.120802.

[35] F. Xing, H. Yu, C. Cheng, Q. Liu, L. Lai, S. Xia, C. Huang, Interfacial microenvironment-regulated cascade charge transport in $Co_6Mo_6C_2$-MoO_2-$CoNC@ZnIn_2S_4$ photocatalyst for efficient hydrogen evolution, Chem. Eng. J. 450 (2022), 138130, https://doi.org/10.1016/j.cej.2022.138130.

[36] H.S. Moon, K.-C. Hsiao, M.-C. Wu, Y. Yun, Y.-J. Hsu, K. Yong, Spatial separation of cocatalysts on Z-scheme organic/inorganic heterostructure hollow spheres for enhanced photocatalytic H_2 evolution and in-depth analysis of the charge-transfer mechanism, Adv. Mater. (2022) 2200172, https://doi.org/10.1002/adma.202200172.

[37] C. Cui, X. Zhao, X. Su, N. Xi, X. Wang, X. Yu, X.L. Zhang, H. Liu, Y. Sang, Porphyrin-based donor–acceptor covalent organic polymer/$ZnIn_2S_4$ Z-scheme heterostructure for efficient photocatalytic hydrogen evolution, Adv. Funct. Mater. (2022) 2208962, https://doi.org/10.1002/adfm.202208962.

[38] J. He, P. Lyu, B. Jiang, S. Chang, H. Du, J. Zhu, H. Li, A novel amorphous alloy photocatalyst (NiB/In_2O_3) composite for sunlight-induced CO_2 hydrogenation to HCOOH, Appl. Catal. B Environ. 298 (2021), 120603, https://doi.org/10.1016/j.apcatb.2021.120603.

[39] Y. Qin, H. Li, J. Lu, Y. Feng, F. Meng, C. Ma, Y. Yan, M. Meng, Synergy between van der waals heterojunction and vacancy in $ZnIn_2S_4$/g-C_3N_4 2D/2D photocatalysts for enhanced photocatalytic hydrogen evolution, Appl. Catal. B Environ. 277 (2020), 119254, https://doi.org/10.1016/j.apcatb.2020.119254.

[40] Y. Luo, B. Deng, Y. Pu, A. Liu, J. Wang, K. Ma, F. Gao, B. Gao, W. Zou, L. Dong, Interfacial coupling effects in g-C_3N_4/$SrTiO_3$ nanocomposites with enhanced H_2 evolution under visible light irradiation, Appl. Catal. B Environ. 247 (2019) 1–9, https://doi.org/10.1016/j.apcatb.2019.01.089.

[41] W. Yu, D. Xu, T. Peng, Enhanced photocatalytic activity of g-C_3N_4 for selective CO_2 reduction to CH_3OH via facile coupling of ZnO: a direct Z-scheme mechanism, J. Mater. Chem. A 3 (2015) 19936–19947, https://doi.org/10.1039/C5TA05503B.

[42] X. Shi, C. Dai, X. Wang, J. Hu, J. Zhang, L. Zheng, L. Mao, H. Zheng, M. Zhu, Protruding Pt single-sites on hexagonal $ZnIn_2S_4$ to accelerate photocatalytic hydrogen evolution, Nat. Commun. 13 (2022) 1287, https://doi.org/10.1038/s41467-022-28995-1.

[43] P. Xia, S. Pan, S. Jiang, J. Yu, B. He, P.M. Ismail, W. Bai, J. Yang, L. Yang, H. Zhang, M. Cheng, H. Li, Q. Zhang, C. Xiao, Y. Xie, Designing a redox heterojunction for photocatalytic "overall nitrogen fixation" under mild conditions, Adv. Mater. 34 (2022) 2200563, https://doi.org/10.1002/adma.202200563.

[44] K. Wang, X. Feng, Y. Shangguan, X. Wu, H. Chen, Selective CO_2 photoreduction to CH_4 mediated by dimension-matched 2D/2D Bi_3NbO_7/g-C_3N_4 S-scheme heterojunction, Chin. J. Catal. 43 (2022) 246–254, https://doi.org/10.1016/S1872-2067(21)63819-6.

[45] K. Chen, X. Wang, Q. Li, Y.-N. Feng, F.-F. Chen, Y. Yu, Spatial distribution of $ZnIn_2S_4$ nanosheets on g-C_3N_4 microtubes promotes photocatalytic CO_2 reduction, Chem. Eng. J. 418 (2021), 129476, https://doi.org/10.1016/j.cej.2021.129476.

[46] K. Zhang, M. Zhou, K. Yang, C. Yu, P. Mu, Z. Yu, K. Lu, W. Huang, W. Dai, Photocatalytic H_2O_2 production and removal of Cr (VI) via a novel Lu_3NbO_7: Yb, Ho/CQDs/$AgInS_2$/In_2S_3 heterostructure with broad spectral response, J. Hazard. Mater. 423 (2022), 127172, https://doi.org/10.1016/j.jhazmat.2021.127172.

[47] X. Bai, X. Wang, T. Jia, L. Guo, D. Hao, Z. Zhang, L. Wu, X. Zhang, H. Yang, Y. Gong, J. Li, H. Li, Efficient degradation of PPCPs by $Mo_{1-x}S_{2-y}$ with S vacancy at phase-junction: promoted by innergenerate-H_2O_2, Appl. Catal. B Environ. 310 (2022), 121302, https://doi.org/10.1016/j.apcatb.2022.121302.

[48] S. Li, Q.L. Mo, S.C. Zhu, Z.Q. Wei, B. Tang, B.J. Liu, H. Liang, Y. Xiao, G. Wu, X. Z. Ge, F.X. Xiao, Unleashing insulating polymer as charge transport cascade mediator, Adv. Funct. Mater. (2022), https://doi.org/10.1002/adfm.202110848.

[49] X. Hui, L. Li, Q. Xia, S. Hong, L. Hao, A.W. Robertson, Z. Sun, Interface engineered Sb_2O_3/$W_{18}O_{49}$ heterostructure for enhanced visible-light-driven photocatalytic N_2 reduction, Chem. Eng. J. 438 (2022), 135485, https://doi.org/10.1016/j.cej.2022.135485.

[50] S. Sharma, V. Dutta, P. Singh, P. Raizada, A. Rahmani-Sani, A. Hosseini-Bandegharaei, V.K. Thakur, Carbon quantum dot supported semiconductor photocatalysts for efficient degradation of organic pollutants in water: a review, J. Clean. Prod. 228 (2019) 755–769, https://doi.org/10.1016/j.jclepro.2019.04.292.

[51] D. Guo, W. Wang, C. Chen, J. He, M. Zhu, J. Chen, C. Zhang, A multi-structural carbon nitride co-modified by Co, S to dramatically enhance mineralization of Bisphenol f in the photocatalysis-PMS oxidation coupling system, Chem. Eng. J. 422 (2021), 130035, https://doi.org/10.1016/j.cej.2021.130035.

[52] Z. Wang, C. Lai, L. Qin, Y. Fu, J. He, D. Huang, B. Li, M. Zhang, S. Liu, L. Li, W. Zhang, H. Yi, X. Liu, X. Zhou, ZIF-8-modified $MnFe_2O_4$ with high crystallinity and superior photo-Fenton catalytic activity by Zn-O-Fe structure for TC degradation, Chem. Eng. J. 392 (2020), 124851, https://doi.org/10.1016/j.cej.2020.124851.

[53] X. Li, J. Xiong, X. Gao, J. Ma, Z. Chen, B. Kang, J. Liu, H. Li, Z. Feng, J. Huang, Novel BP/BiOBr S-scheme nano-heterojunction for enhanced visible-light photocatalytic tetracycline removal and oxygen evolution activity, J. Hazard. Mater. 387 (2020), 121690, https://doi.org/10.1016/j.jhazmat.2019.121690.

[54] B. Kraeutler, A.J. Bard, Heterogeneous photocatalytic synthesis of methane from acetic acid - new Kolbe reaction pathway, J. Am. Chem. Soc. 100 (1978) 2239–2240, https://doi.org/10.1021/ja00475a049.

[55] K. Hashimoto, T. Kawai, T. Sakata, Photocatalytic reactions of hydrocarbons and fossil fuels with water. Hydrogen production and oxidation, J. Phys. Chem. 88 (1984) 4083–4088, https://doi.org/10.1021/j150662a046.

[56] I. Izumi, F.-R.F. Fan, A.J. Bard, Heterogeneous photocatalytic decomposition of benzoic acid and adipic acid on platinized titanium dioxide powder. The photo-Kolbe decarboxylative route to the breakdown of the benzene ring and to the production of butane, J. Phys. Chem. 85 (1981) 218–223, https://doi.org/10.1021/j150603a002.

[57] S. Li, C. Wang, M. Cai, F. Yang, Y. Liu, J. Chen, P. Zhang, X. Li, X. Chen, Facile fabrication of TaON/Bi_2MoO_6 core–shell S-scheme heterojunction nanofibers for boosting visible-light catalytic levofloxacin degradation and Cr(VI) reduction, Chem. Eng. J. 428 (2022), 131158, https://doi.org/10.1016/j.cej.2021.131158.